UNIVERSITY OF CALIFORNIA, SAN DIEGO

Issues related to the characterization and fabrication of coiled carbon nanotube based inductors

A dissertation submitted in partial satisfaction of

the requirements for the degree Doctor of Philosophy

in

Electrical Engineering (Nanoscale Devices and Systems)

by

Hasan Mohammad Faraby

Committee in charge:

Prabhakar Bandaru, Chair
Yu-Hwa Lo, Co-Chair
Michael DiBattista
Michael Fogler
Yuan Taur
Jie Xiang

2014

The dissertation of Hasan Mohammad Faraby is approved, and it is acceptable in quality and form for publication on microfilm and electronically:

_____

_____

_____

_____

_____
Co-Chair

_____
Chair

University of California, San Diego

2014

DEDICATION

This dissertation is dedicated to my wife and my family.

TABLE OF CONTENTS

LIST OF FIGURES

LIST OF TABLES

ACKNOWLEDGEMENTS

First of all, I would like express my sincere gratitude to my Advisor, Prof. Prabhakar Bandaru, for his guidance and support throughout my entire Ph.D. career. His vast experience and thorough knowledge was the key to my development as a successful researcher. He would always provide advice and creative solutions to any problems I faced and always kept me encouraged whenever, I had difficulties throughout my Ph.D. career.

I would also like to convey a very special thanks to my Mentor and Doctoral Committee member: Dr. Michael DiBattista for the constructive suggestions and guidance he provided.

I would also like to thank my Co-Chair Prof. Yu-Hwa Lo and Doctoral Committee members: Prof. Michael Fogler, Prof. Yuan Taur, and Prof. Jie Xiang for the constructive suggestions and guidance they provided.

I would like to thank Dr. Steve Pfeifer, Dr. Paothep Pichanusakorn and Anna Alexander for their participation and the insightful discussions on various projects.

I would like to thank Dr. Max Aubian, Dr. Rahul Kapadia, Byung Kim, Krishna Vemuri, Rajaram Narayanan, David Moreira, Hidenori Yamada and Thomas Hall for the support they have provided over the many years

I would also like to thank Corey Senowitz, Theresa Graupera and Roddy Cruz all from Qualcomm Technologies Inc., for the trainings, tricks and suggestions they provided regarding my research.

I also need to thank the Nano3 staff for the excellent support they provided which made my research possible: Larry Grissom, Sean Parks, Ivan Harris, Dr. Xuekun Lu, Dr. Ahmet Erten, Ryan Anderson, Dr. Maribel Montero, and Dr. Bernd Fruhberger.

Most importantly I would like to thank my wife and my family for their constant encouragement during my academic career. They were always there whenever I felt discouraged or had any kind of problems.

Portions of Chapter 2 are a reprint of material as it appears in the following publications: Faraby H, Bandaru PR. "High Energy Density, High Operating Frequency and Energy Efficient On-Chip Inductors based on Coiled Carbon Nanotubes (CCNTs)." *MRS Online Proc Libr*. 2013;1551. Faraby HM, Rao AM, Bandaru PR. "Modeling High Energy Density Electrical Inductors Operating at THz Frequencies Based on Coiled Carbon Nanotubes." *Electron Device Lett IEEE*. 2013;34(6):807–809. doi:10.1109/LED.2013.2258454. The dissertation author was the primary investigator and author of this material.

Portions of Chapter 3 are a reprint of materials as it appears in the following publications: Faraby H, DiBattista M, Bandaru PR. "Percolation of gallium dominates the electrical resistance of focused ion beam deposited metals" *Appl Phys Lett*. 2014;104(17):173107. doi:10.1063/1.4874342. Michael DiBattista, Hasan Faraby, Corey Senowitz, Prabhakar Bandaru, "Using Energy Dispersive Spectroscopy (EDS) to Determine the Resistance of FIB Jumpers for Circuit Edit" *Proc. of International Sym. on Testing and Failure Analysis, 2014.*The dissertation author was the primary investigator and author of these materials.

Portions of Chapter 4 are a reprint of material as it is under preparation for publication: Faraby H, DiBattista M, Bandaru PR. “Comparison of the electrical capacitance characteristics of SiO_2 deposited through gallium and xenon based focused ion beam systems.” The dissertation author was the primary investigator and author of this material.

VITA

2008 Bachelor of Science, Bangladesh University of Engineering & Technology
Electrical and Electronic Engineering

2011 Master of Science, University of California, San Diego
Electrical Engineering (Nanoscale Devices and Systems)

2014 Doctor of Philosophy, University of California, San Diego
Electrical Engineering (Nanoscale Devices and Systems)

PUBLICATIONS

1. H M Faraby, A M Rao, and P R Bandaru, "Modeling high energy density electrical inductors operating at Thz frequencies based on coiled carbon nanotubes", *IEEE-Electron Device Letters, Vol. 34, Issue 6.*

2. H Faraby and P Bandaru, "High energy density, high operating frequency and energy efficient On-Chip inductors based on Coiled Carbon Nanotubes (CCNTs)", *in proceedings of 2013 Materials Research Society Spring Meeting, April, 2013.*

3. H Faraby, Michael DiBattista and P R Bandaru, "Percolation of gallium dominates the electrical resistance of focused ion beam deposited metals", *Applied Physics Letters, Vol.104, Issue 17.*

4. Michael DiBattista, Hasan Faraby, Corey Senowitz, Prabhakar Bandaru, "Using Energy Dispersive Spectroscopy (EDS) to Determine the Resistance of FIB Jumpers for Circuit Edit", *Proc. of Intl. Sym. on Testing and Failure Analysis, 2014*

5. H Faraby, Michael DiBattista and P R Bandaru, "Comparison of the electrical capacitance characteristics of SiO_2 deposited through gallium and xenon based focused ion beam systems", *under preparation*

ABSTRACT OF THE DISSERTATION

Modeling Coiled Carbon Nanotube Inductors and the Resistivity of Focused Ion Beam Deposited Metals and Insulators

by

Hasan Mohammad Faraby

Doctor of Philosophy in Electrical Engineering (Nanoscale Devices and Systems)

University of California, San Diego, 2014

Professor Prabhakar Bandaru, Chair

The superior inductive properties of coiled carbon nanotubes (CCNTs) have been demonstrated through numerical computations. It is shown, through computations, that a range of inductance values (in the pH to μH range) operational at THz frequencies could be obtained through a variation of CCNT geometric parameters, which can be accomplished through rational synthesis. A comparison of the proposed inductor material

to conventional inductor material *e.g.* copper (Cu), in terms of both component footprint and material volume, indicated a greater quality factor (Q) through the use of the CCNTs. Experimental characterization of these CCNT inductors require high quality ohmic contacts. Focused ion beam based metal deposition is one of the easiest ways to create contacts on those nanostructures.

Metal deposition with focused ion beam (FIB) systems result in material composed of carbon, oxygen, gallium and the primary metal from the metallo-organic precursor. Four point probe measurements to determine the material resistivity and energy dispersive spectroscopy (EDS) to determine the relative chemical composition were conducted on a wide range of FIB deposited platinum (Pt) and tungsten (W) lines. It has been shown that the gallium (Ga) percentage in the metal line plays a significant role in reducing the electrical resistivity of the material.

Effective media theory (EMT), specifically using Mc Lachlan's general effective medium (GEM) equation is used to describe the relationship between the chemical compositions of the FIB deposited metal lines and the corresponding electrical resistivity. The relation between the chemical elements and the resistivity of the FIB deposited metal lines will make possible the accurate estimation of their resistance without using conventional probe stations.

Like metals insulators can also be deposited using the FIB system. Insulator deposition by FIB systems results in SiO_2 layers with impurities from gallium (Ga) and carbon (C). The electrical capacitance of focused ion beam (FIB) deposited SiO_2 is shown to be sensitive to the specific composition of the ion beam. The effect of Ga

contamination can be identified by comparing the electrical properties of similar depositions by plasma FIB. In the plasma FIB xenon (Xe) ion plasma is used as the ion source instead of Ga. The presence of carbon, inevitably found as the product of the hydrocarbon precursor decomposition has been isolated as a major cause for an observed decrease in the capacitance/effective dielectric constant of the SiO_2. Our study has implications to the deposition of high quality insulator films through FIB based methodologies.

In this way detailed investigation of the origin of the resistivity of FIB deposited metals and insulators provided significant insights on the contact resistance of the FIB contacts to the CCNTs , which was prohibiting the true experimental characterization of the inductive properties of CCNTs inductors.

Chapter 1 Introduction

This chapter describes the background information about inductors and focused ion beam based depositions. It discusses the current challenges of inductor design, the impact of focused ion beam deposition and describes the process.

1.1 Inductors

Inductors are one of the three fundamental components in *any* electrical circuit. It is a passive two-terminal electrical component which resists changes in electric current passing through it. It consists of a conductor such as a wire, usually wound into a coil. When a current flows through it, energy is stored temporarily in a magnetic field in the coil. When the current flowing through an inductor changes, the time-varying magnetic field induces a voltage in the conductor, according to Faraday's law of electromagnetic induction, which opposes the change in current that created it. Inductors are a fundamental element in high frequency circuits for wireless applications such as power amplifiers, low noise amplifiers, matching networks, on-die antennas, LC tank circuits, and many others[1,2](Figure 1.1). However, it has been often discussed that there has been essentially no change in inductor design over the past 40 years[3].

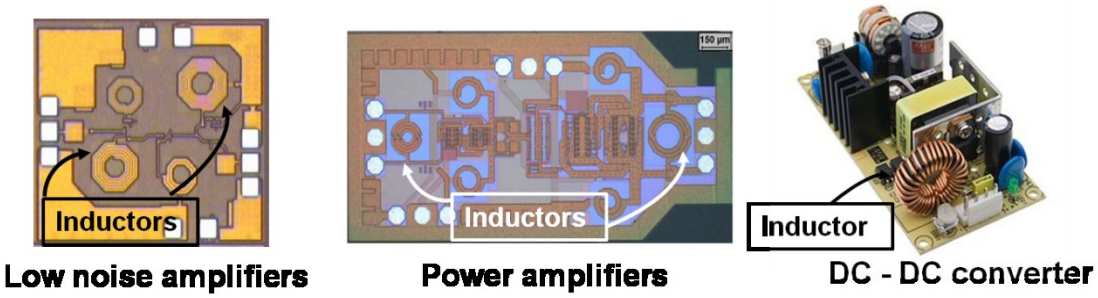

Figure 1.1: Various devices using inductors[4,5]

1.2 Important Figure of Merits & Definitions

There are three parameters that characterize an inductor at a given frequency ($f = \omega/2\pi$). They are:

- **Inductance (L) :**

  It determines the amount of energy that can be stored in the inductor. It is measured in units of Henry(H). Current inductor for electronics applications can have inductance from 1nH to 10μH.

- **Quality factor ($Q = \omega L/R$):**

  The quality factor is the ratio of L to R times angular frequency and is an important performance metric in inductor design. Parasitic resistance determines the Q factor, basically Q is inversely proportional to the power loss or resistance. The parasitic resistance can be further broken down into the direct current (DC) resistance of the inductor, the resistance due to the skin effect which is the tendency of an alternating electric current (AC) to become distributed within a conductor such that the current

density is largest near the surface of the conductor, and decreases with greater depths in the conductor. The electric current flows mainly at the "skin" of the conductor, between the outer surface and a level called the skin depth, the resistance due to eddy current excitation, which are electric currents induced within conductors by a changing magnetic field in the conductor, these circulating eddies of current have inductance and thus induce magnetic fields. These fields can cause repulsion, attraction, propulsion, drag, and heating effects, and dielectric loss which is the leakage current that flows through the dielectric material, in the substrate. The DC resistance increases as the size of the interconnect decreases. Such effects are so large that on chip inductors utilize a thick metal layer to decrease the resistance, but at a cost of a substantially increased device foot print[6]. Traditional inductor materials have increased resistance at high frequencies (e.g. 10s of GHz) due to the skin effect. This results in lower Q factor and limited frequency ranges for presently used inductors. As a result, a miniaturized inductor with a high Q factor and operating frequency is very desirable.

- **Self resonant frequency ($f_{SR} = 1/2\pi\sqrt{LC}$):**

The self resonant frequency is the highest operating frequency of the inductor. Parasitic capacitances determine the self resonant frequency because the capacitive reactance decreases with increasing frequency and the inductive reactance increases with increasing frequency, so at high frequencies the more current tends to flow through the low reactance path making the circuit less inductive. Currently f_{SR} is limited to ~ 40GHz.

1.3 Current Challenges in Inductor Design in Wireless Applications

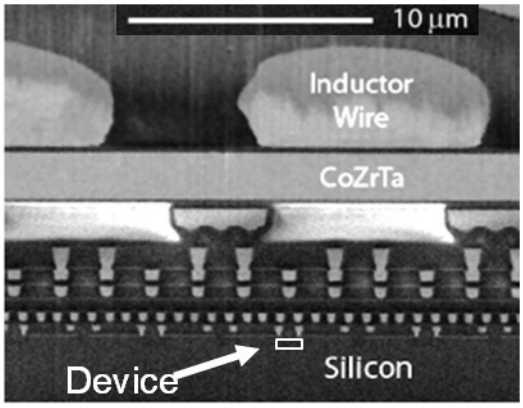

Figure 1.2: Comparison of inductor wire and device size[7]

There are four main design challenges, these include:

- **Size and Cost:**

Inductor development in integrated circuits constantly lags behind development of other circuit elements. The first challenge is to reduce the size and the cost. Figure 1.2 is an image of a semi-conductor device with an integrated inductor on the top side. The image is a cross-section of the device showing interconnects and location of the transistors (device) in the silicon substrate. As seen from Figure 1.2 that the device size has reduced drastically compared to the inductor wire, so when both of them are integrated on the same chip, the size and cost of the chip is affected by the size of the inductor. We can also see from Figure 1.1 that inductors take up a significant amount of space on various microelectronic devices. So inductor design needs to be scaled down to reduce the cost and the size of the chip.

- **100 GHz applications:**

The second challenge is regarding the magnitude of inductance, generally copper inductors are available in the range of few nano Henries to few hundreds of nano Henries, but for MEMS and 100GHz applications, we need inductors in the range of few pico Henries to hundreds of pico Henries. Copper technology adequately makes nano Henry inductors, but has struggled at making inductances at the pico Henry values desired by industry.

- **High Quality factor:**

Power consumption and device efficiency are extremely important design parameters, particularly in battery powered devices. High quality factor relates to increased efficiency, and thus improvements to the quality factor are necessary as users and consumers demand lighter, less power hungry devices.

- **THz Operating frequency:**

The last challenge is to achieve THz operating frequency. The higher the operating frequency is, the faster the data transfer rates and overall computational speeds are. As a result, higher operating frequencies are preferred. However, copper based technology has a maximum operating frequency in the 10s of gigahertz, and the performance and efficiency degrade well before the maximum operating frequency. As a result, new technology is required for the next generation of high frequency electronics.

1.4 Current Challenges in Inductor Design for Power Electronics Applications

The design of inductors in power electronic circuits, has remained essentially unchanged for 40 years. Inductors in these applications require high inductance values and high current carrying capacities. This results in large inductors, whose size, particularly in comparison to the rest of the device makes them the heaviest and most expensive part of the device. Thus, as seen in Figure 1.3, you can either get high inductance, with a large resulting footprint and poor high frequency efficiency, or you can decrease the footprint of the device, and improve the high frequency efficiency, while decreasing the inductance. However, even with these compromises, the high inductances are not particularly high for power applications, and the small footprints and small inductances are not small enough for many integrated circuit applications.

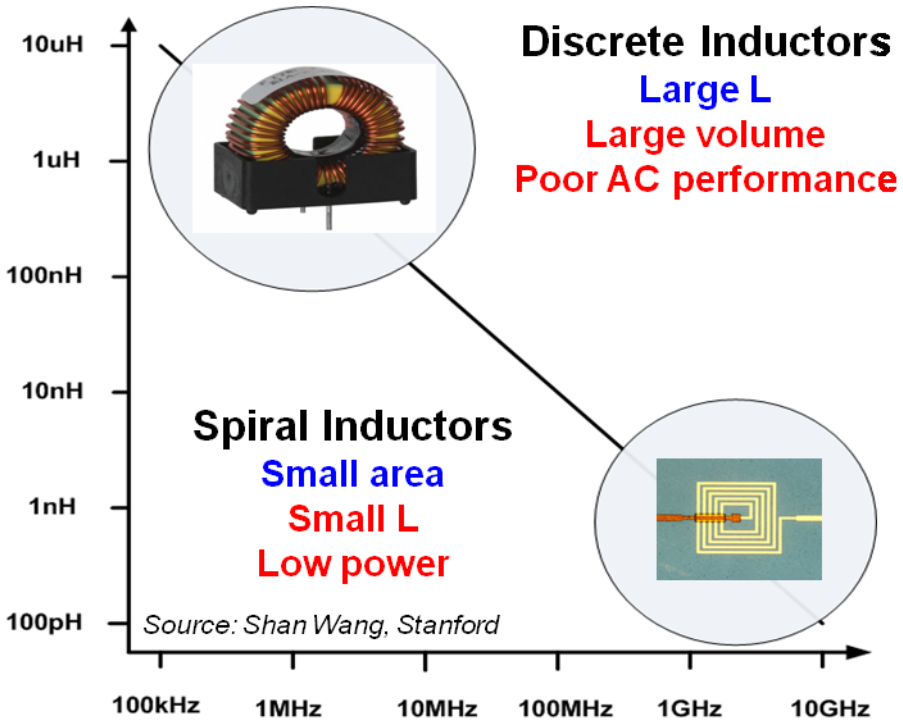

Figure 1.3: Inductance vs frequency

Copper based technology thus struggles both at making very low inductance inductors and high inductance inductors at practical or useful sizes. This lack of development has made it difficult to improve things such as overall size, and weight of the device without improvements to the inductor technology, which copper has thus far been unable to provide.

1.5 Solution to Current Challenges

To overcome these challenges we would like to propose coiled carbon nanotubes rather than copper as inductor elements. CCNTs are multi walled carbon nanotubes coiled in a spring or solenoid like shape. Each of the shells of the multiwall CNT is one atom thick and they are separated from each other by 0.34nm (atomic level spacing).

The unique feature of these nanotubes is their kinetic inductance, which is due to the nanoscale properties of the nanotubes. When current flows through a 1D conductor

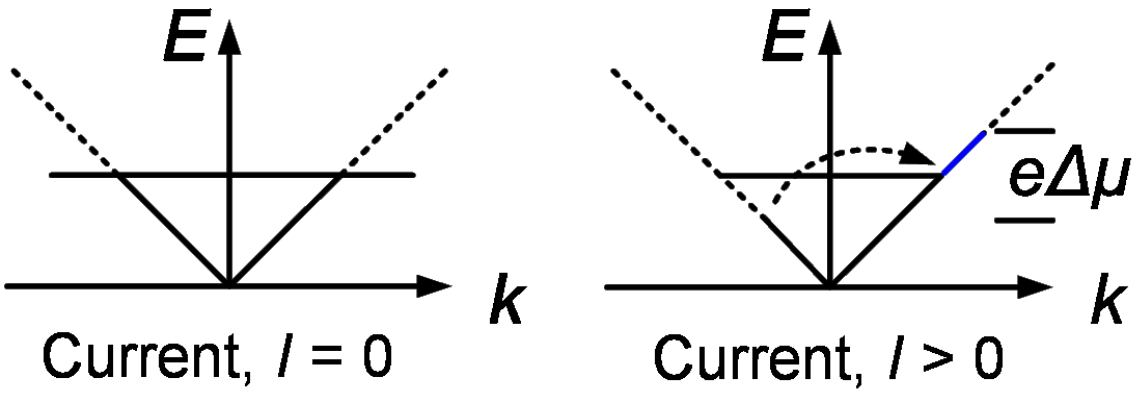

Figure 1.4: Energy vs wave vector diagram of a 1D conductor with and without current flow

such as the individual shells of a multi wall carbon nanotube, the current carrying electrons contain high kinetic energy. This is due to the quantum confinement effect which makes the available energy states in the 1D conductor discrete and higher than the bulk conductors, during current conduction the electron occupy those high energy states and we get additional energy storage capacity in the form of kinetic energy(Figure 1.4). That kinetic energy is equated to the inductive energy to give us kinetic inductance. This effect is only observed at nano-scale dimensions. In bulk conductors available electron energy levels are not discrete so we cannot get significant kinetic inductance from bulk conductors. Due to their coiled shape they also have magnetic inductance like that of typical solenoids. The basic difference between kinetic inductance and magnetic inductance lies in the form of energy storage, i.e. in kinetic inductance the energy is stored in the form of kinetic energy and in magnetic inductance the energy is stored in the magnetic field.

Another key feature of CCNTs are that the inductance value can be tuned based on four key parameters. They are:

- Coil radius(r_{out}),
- Tube radius(c),
- Pitch(P) and
- Number of turns (N_t).

The total inductance of the CCNTs is expressed as the sum of their magnetic inductance and kinetic inductance. The synthesis process of the CCNTs are described in Chapter 2.

1.6 Creating Contacts to CCNT Inductors

In order to accurately characterize and verify the properties of CCNT inductors, we need to establish excellent ohmic contacts to those nanostructures. But creating ohmic contacts of carbon nanotubes is not straight forward. The biggest issue in determining the inductive properties of CCNTs is contact resistance. Numerous efforts are still underway to establish the perfect ohmic contact to nanostructures. One of them is using focused ion beam based material deposition. We created contacts to the CCNT using this method and analyzed multiple devices but all the measurement results showed very high contact resistance which was dominating the behavior of the CCNTs.

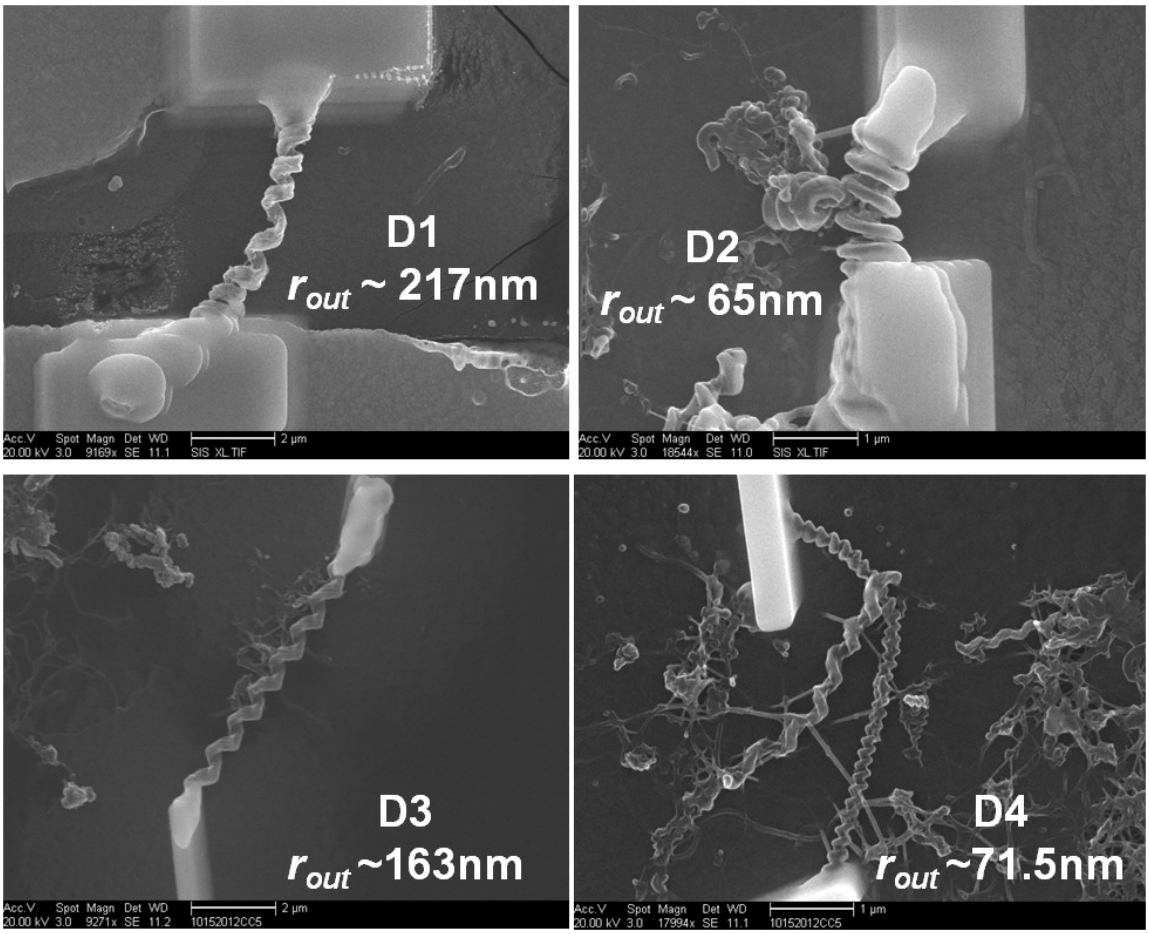

Figure 1.5: Analyzed CCNT devices contacted with FIB

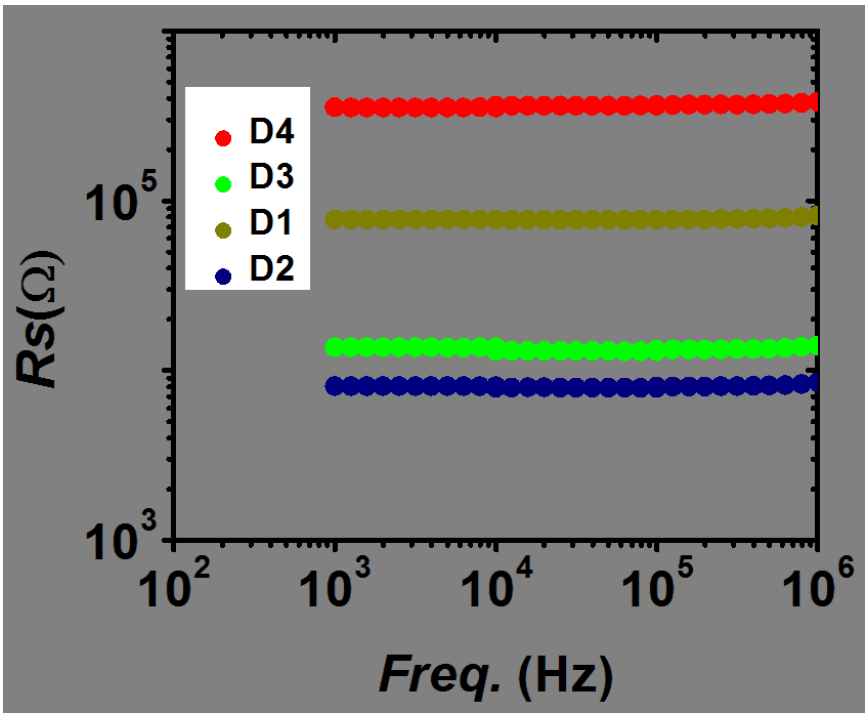

Figure 1.6: Series resistance vs. frequency

Figure 1.5 shows SEM images of the analyzed devices with FIB contacts. It also shows the measured tube radius (r_{out}). Figure 1.6 illustrates the series resistance with respect to the voltage source frequency of the analyzed devices. We see that all the devices show very high resistance which is dominating their behavior instead of inductance.

In order to understand the origin of this high resistance we investigated the resistivity of FIB deposited metals. The following section will describe FIB based metal deposition process, its impact to semiconductor industry and various aspects of it.

1.7 Focused Ion Beam (FIB) Based Deposition

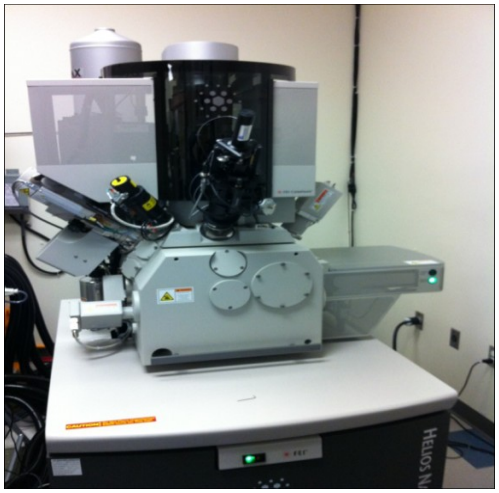

Figure 1.7: FEI Helios Nanolab FIB System

A focused ion beam tool is a scientific tool similar in concept to the more widely known scanning electron microscope (SEM). With a FIB system the charged particle is an ion, often gallium instead of electron, a high voltage accelerates the ion, which allows them to sputter away material when they are accelerated towards the surface. FIBs are powerful tools (Figure 1.7) because they can deposit and remove metal with high precision. Some of the FIB tools are equipped with two beams, one composed of electrons which is primarily used for imaging and energy dispersive spectroscopy, and the other is composed of ions, which is used to cut and connect circuitry with in a chip, as well as to create probe points for electrical test. The basic principle here is to decompose an organo-metallic precursor using the energy of the ion beam to deposit metal on the substrate. Depending on the precursor gas various metals or insulators can be deposited such as Pt, W, Mo, Cu, or SiO_2 or if the precursor gas is an etchant, such as I_2, Cl_2, Xe, XeF_2, etc we can perform etching operation. For our experiments we used two types of FIB tools, one of them uses gallium as the ion beam which is generated from the liquid

metal ion source (LIMS)(Figure 1.9) where the ion beam is generated from a point source and the other one uses xenon (Xe) as the ion beam which is generated from an inductively coupled plasma ion source(Figure 1.8). One of the main advantages of Xe based plasma FIB is that it allows us to separate the impact of Ga contamination in our depositions. Since Xe is gaseous at room temperature it cannot be present as an impurity in the depositions. By comparing electrical properties of the depositions from Ga and Xe base FIB, we can understand the effect of Ga. Another advantage is of Xe based plasma FIB that they can have beam current in the range of μAs where as the Ga FIB can go up to nAs. This gives a speed advantage, during high volume milling operation to the Xe plasma FIB.

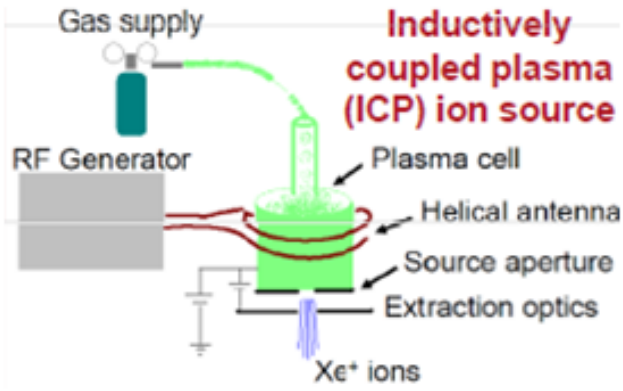

Figure 1.8: Schematic of ICP ion source used in Xe based Plasma FIB[8]

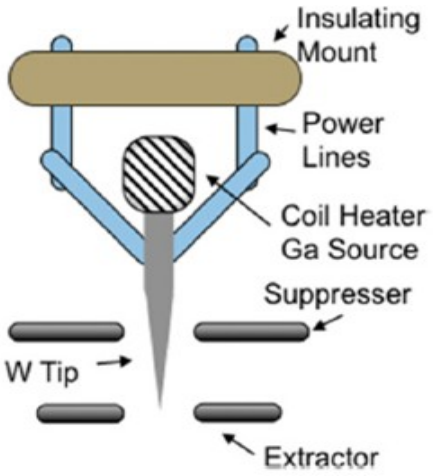

Figure 1.9: Schematic of Liquid Metal ion source used in Ga based FIB[9]

Due to the fundamental difference in ion beam generation mechanism we get much higher beam current in the Xe based plasma FIB tools.

1.8 Impact of FIB Circuit Edit (CE)

As semiconductor device scaling advances according to Moore's Law, focused ion beam (FIB) nano-deposition capabilities are critical to the debug and repair of complex circuitry. FIB based machining and metal deposition enable a variety of circuit and interconnect rewiring operations in the prototyping stage of integrated circuit (IC) design and manufacturing, thus reducing product development cycle time. One of key capabilities behind FIB involves using the energy from an ion beam to decompose an organo-metallic precursor to selectively deposit metal on a substrate.

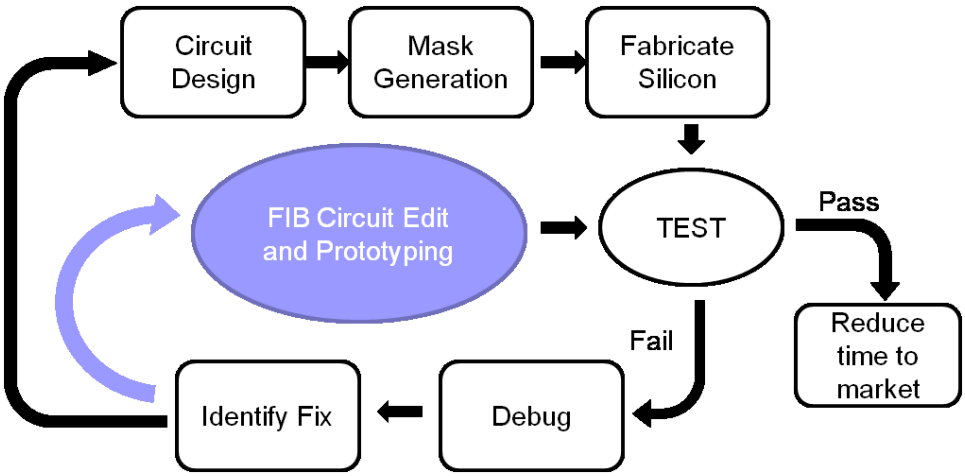

Figure 1.10: Impact of FIB based circuit edit

Figure 1.10 shows the benefit of using FIB circuit edit during product development. Generally the development cycle goes like this: First the chip is designed then masks are made, and silicon is fabricated after that the part is tested for the first time. Once a problem is found and a fix is determined, it must be validated before becoming part of the final design. This means that the design must be modified and new chips manufactured. This process can take weeks to months to find out whether the fix is correct. With FIB CE, the fix can be implemented within a day right on the chip and then tested, providing immediate feedback. Several fixes can be collected before committing to new silicon. In this way FIB based CE can save the cost of mask and reduce the time to market, now as the device sizes are scaled down day by day the cost of mask is increasing so FIB based CE is becoming more important but the resistivity of FIB deposited metals are ~100 times higher than the bulk metal consequently, the relationship of the chemical composition and structure to the electrical resistivity of FIB deposited metals needs to be

quantified, to drive further improvements in the debug of ICs where lower resistance values of interconnects, with concomitantly reduced power, are necessary.

1.9 FIB based material deposition process

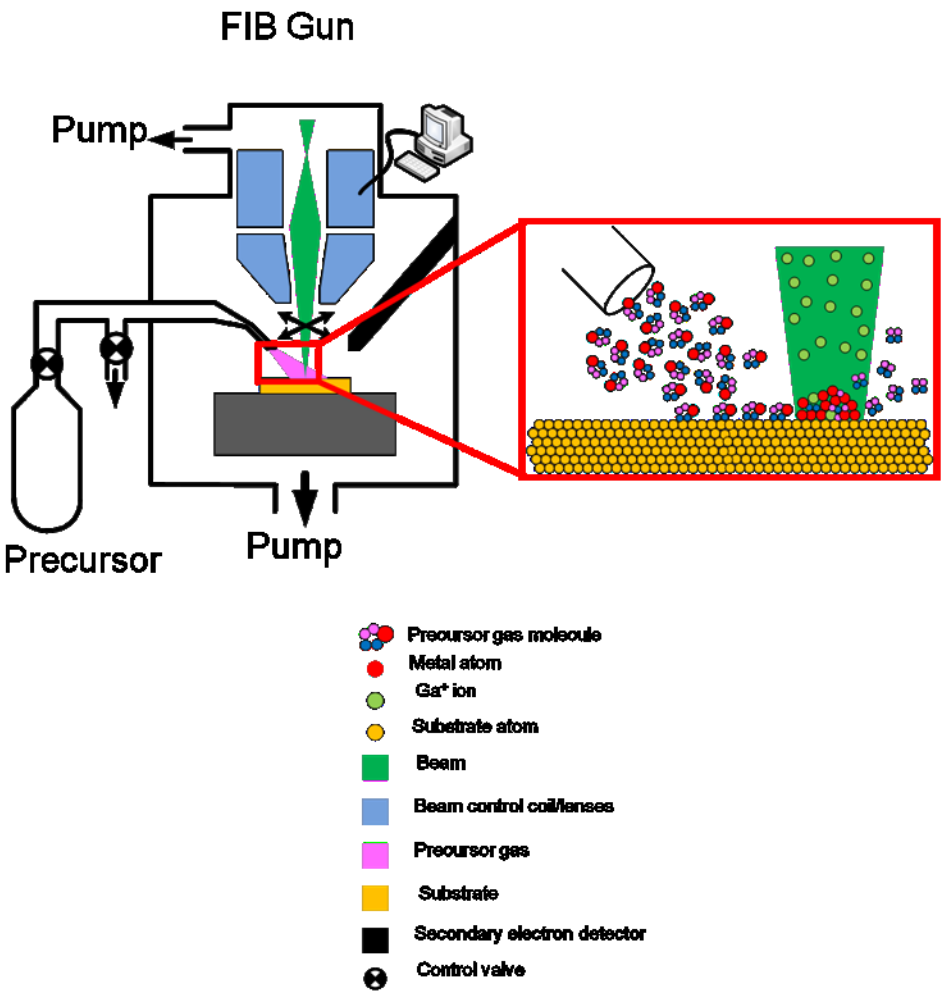

Figure 1.11: FIB Deposition Mechanism

Figure 1.11 is a simplified block diagram of FIB based metal deposition. The ion beam is generated from a point source in the FIB gun which is guided by computer controlled electrostatic lenses that focus and raster it on the substrate surface according to a desired pattern. The beam path and raster area are obtained from user inputs to a computer, connected to the beam controlling coils/lenses. The FIB gun is mounted on a vacuum chamber coupled to the motion controlled sample stage and precursor gas injection system (GIS). Generally the GIS includes a pressure controlled reservoir that can be heated or cooled which is connected to a fine nozzle with diameter around 0.5 mm. The open end of the nozzle can be brought into close proximity to the substrate surface on which the ion beam is focused. During metal deposition, metal containing precursor gases are adsorbed by substrate atoms, then high energy ion beam dissociates the metal atom and deposit them on the substrate and residual gases leave the deposition chamber.

A significant amount of impurity atoms such as carbon and gallium also get deposited during this process. We would like to see the influence of those impurities on the resistivity of the deposited metals.

1.10 Preliminary Experiment

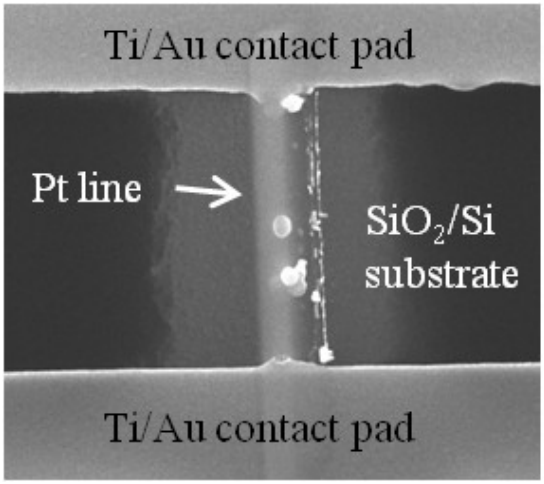

Figure 1.12: SEM Image of a FIB deposited Pt metal line

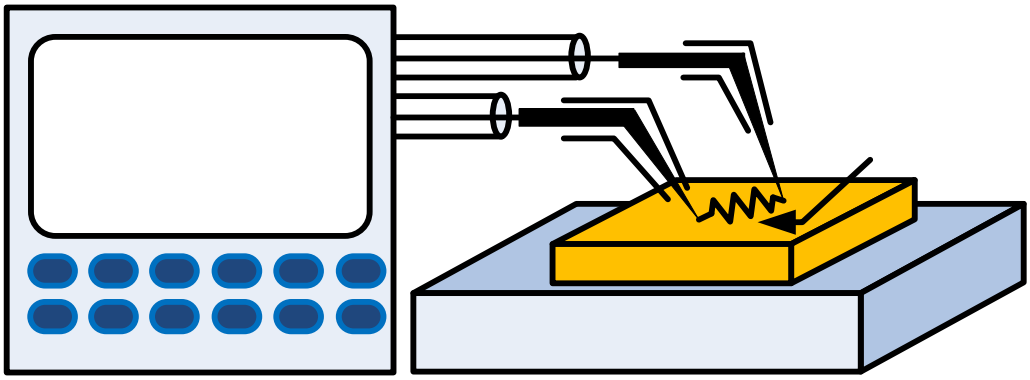

Figure 1.13: Schematic of the measurement setup

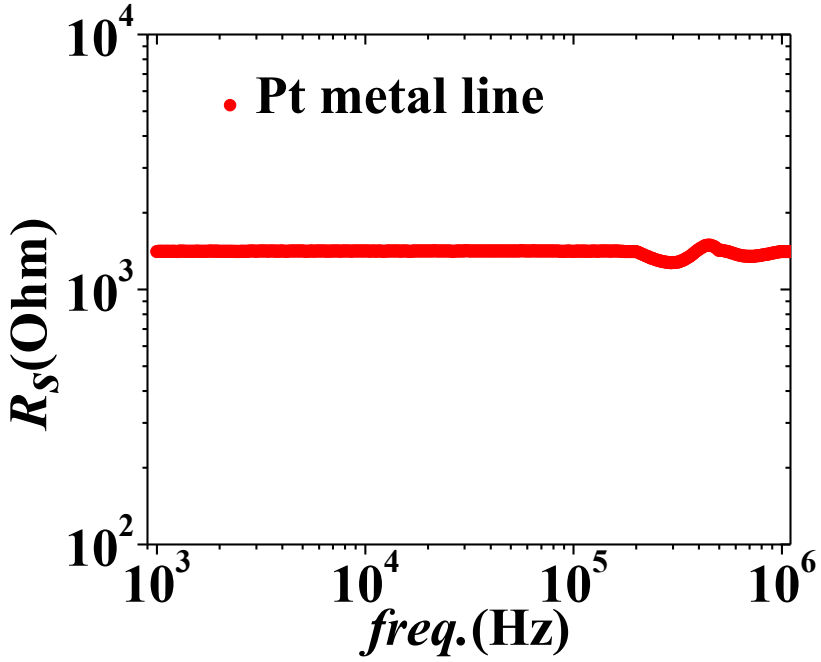

Figure 1.14: Series resistance (R_s) vs *freq.* of the Pt metal line

For preliminary experimentation, Pt metal lines (Figure 1.12 using FIB (Ga^+) with standard used deposition parameters on a SiO_2/Si substrate between Ti/Au contact fingers was deposited and the series resistance (R_s) (Figure 1.14) of the structure was measured. The calculated resistivity of Pt, assuming ideal contacts, form the experiment was *indeed two orders of magnitude* larger than the published bulk values, which *warrant detailed investigation* of FIB deposited metal lines to improve its resistivity.

Chapter 2 Coil Carbon Nanotube Inductors

This chapter will describe how to estimate the inductance of CCNT inductors and compare it with conventional Copper inductors with respect to different figures of merit.

2.1 Introduction

We discuss the inductance, using quantum mechanical characteristics of rationally synthesized coiled carbon nanotubes (CCNTs) to harness high inductor performance, with small device footprint.

We will show the potential of CCNTs to drastically reduce limitations of conventional inductors, extending f_{SR} up to 10 THz. The foundation is their superior current carrying capacity (of the order of 10^9A/cm^2, two orders of magnitude larger than copper) with low electrical resistance and negligible parasitic due to coiled geometry, along with the harness of the kinetic inductance (L_k), in addition to electromagnetic inductance (L_{em}). Moreover, an individual atomic layer thick CNT/Graphene sheets would not be susceptible to the skin effect.

2.2 Computational Details

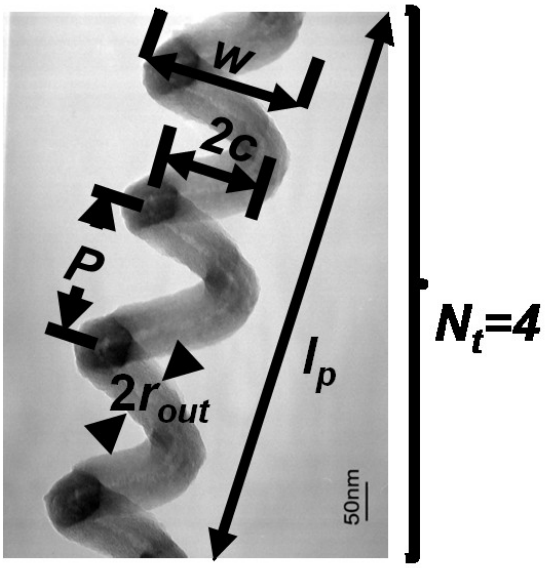

Figure 2.1: SEM image of a CCNT denoting width(w), outer tube radius(r_{out}), pitch(P),coil radius(c), projected length(l_p) and number of turns(N_t))

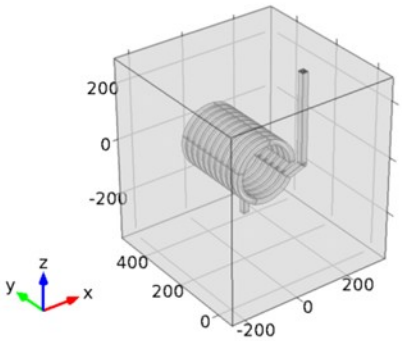

Figure 2.2: The CCNT structure used in finite element simulation with r_{out}=10nm, c=100 nm, P=30 nm, and N_t =10

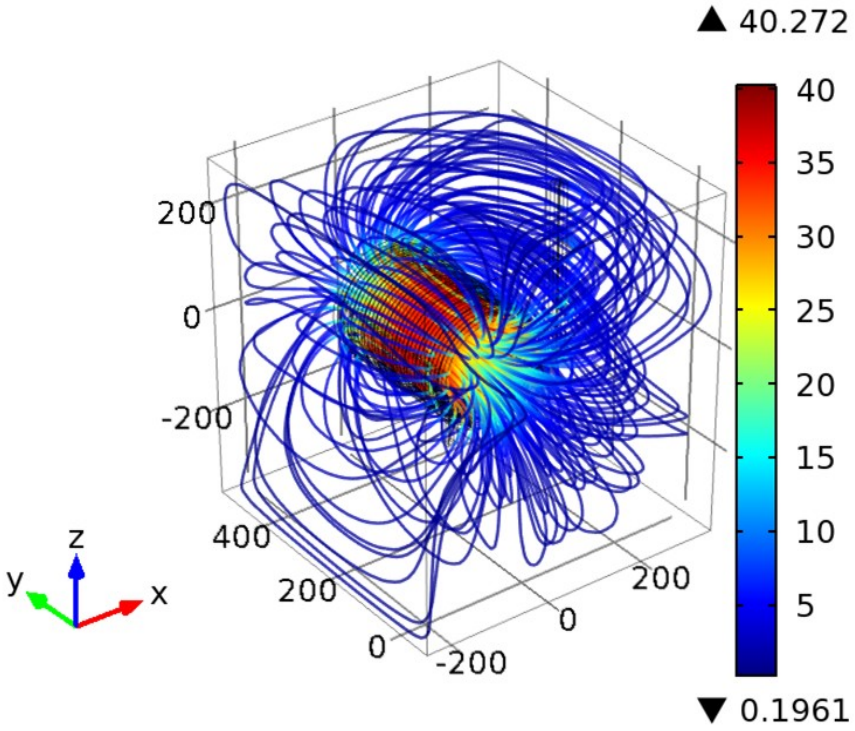

Figure 2.3: Magnetic flux density in units of nT of the CCNT structure

We modeled the CCNT as a metallic multiwall CNT with the following four geometric parameters defined in Figure 2.1, *i.e.,*

(i) tube radius, r,

(ii) coil radius, c,

(iii) pitch, P, and

(iv) number of turns, N_t.

When electrical current (I) is passed, the electromagnetic inductance (L_{em}) would comprise contributions from flux linkage *interior* and *exterior* to the CCNT, *i.e.,* $L_{M,int}$ and $L_{M,ext}$, respectively. The CCNT was modeled as a tube with an inner and outer radius (r_{in} = 5 nm and r_{out} = 10 nm) as in Figure 2.2, with an extended/total length, l_t and an

coiled/projected length, l_p, and the inductances/unit length were estimated (assuming the CCNT to be akin to a long solenoid[10], as l_p is typically greater than three times c) through:

$$L_{M,int} = \left(\frac{\mu}{2\pi \left(r_{out}^2 - r_{in}^2 \right)^2} \right) \left[\frac{r_{out}^4 - r_{in}^4}{4} - r_{in}^2 \left(r_{out}^2 - r_{in}^2 \right) + r_{out}^4 \, ln \left(\frac{r_{out}}{r_{in}} \right) \right] \tag{2.2.1}$$

$$L_{M,ext} = \frac{\pi \mu c^2 N^2}{l_p^2} \tag{2.2.2}$$

The results obtained by (2.2.1) and (2.2.2) were confirmed by numerical simulations using COMSOL® Multiphysics; where Maxwell's equations were solved using finite element method in a quasi-static approximation as the dimensions of the CCNT are significantly smaller than the wave length of the EM wave (Figure 2.3). The simulated inductance of a CCNT with typical length scales of r_{out}=10nm, c=100 nm, P=30 nm, and N_t =10 was 10pH and the EM inductance estimated from equations (2.2.1) and (2.2.2) above was ~11pH. A substantially additional contribution, to the net inductance, would be from the constituent one-dimensional single wall nanotubes (SWNTs) through their kinetic inductance (L_k)[11,12,13] which arises through a consideration that electrons can circulate in loops internal to the wire. The resultant current (I) flow depends on the excess number of electrons moving in one direction compared to the other. For example, at the nano-scale(say, < 5nm), the energies of electrons are quantized and only the excess electrons occupying the high energy states contribute to the current flow, the kinetic energy is then equivalent to $\frac{1}{2} L_k I^2$. Considering that each electronic channel of

conduction would contribute to L_k, we enumerate the total number of channels (N_{chan}) for a given CCNT diameter. This may be done through counting the number of occupied modes (M) for a single constituent SWNT and then summing over the multiple SWNTs (m) that comprise the CCNT through:

$$N_{chan} = \sum_i^m \sum_j^M f_j \tag{2.2.3}$$

where f_j $(=1/(1+exp(|E_j-E_F|/k_BT)))$ is the Fermi-Dirac function. The m would be proportional to the r_{out}, and consequently a relationship of the form:

$$N_{chan} = a \cdot r_{out} + b \tag{2.2.4}$$

with a =0.1224 nm^{-1} and b=0.425 was assumed[14]. The L_k per unit length can then be derived to be: $h/4v_Fe^2N_{chan}$, where h is the Planck constant, v_F is the Fermi velocity, and e the elementary electronic charge. Such a relation for L_k was experimentally shown to be correct for SWCNTs for frequencies above 10GHz[11] and indeed, previous simulations[15] have shown L_k independent of frequency above 200GHz. So the net inductance, L_{net} (incorporating both classical and quantum effects) was expressed through:

$$L_{net} = l_t \cdot L_{M,int} + l_p \cdot L_{M,ext} + l_t \cdot L_k \tag{2.2.5}$$

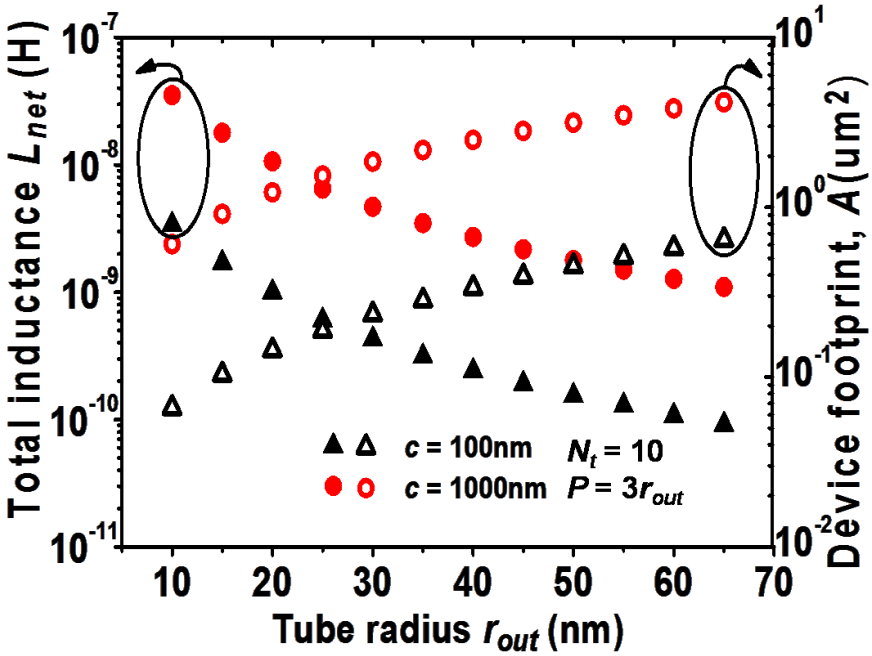

Figure 2.4: L_{net} and A vs. r_{out} at c = 100nm and 1000nm

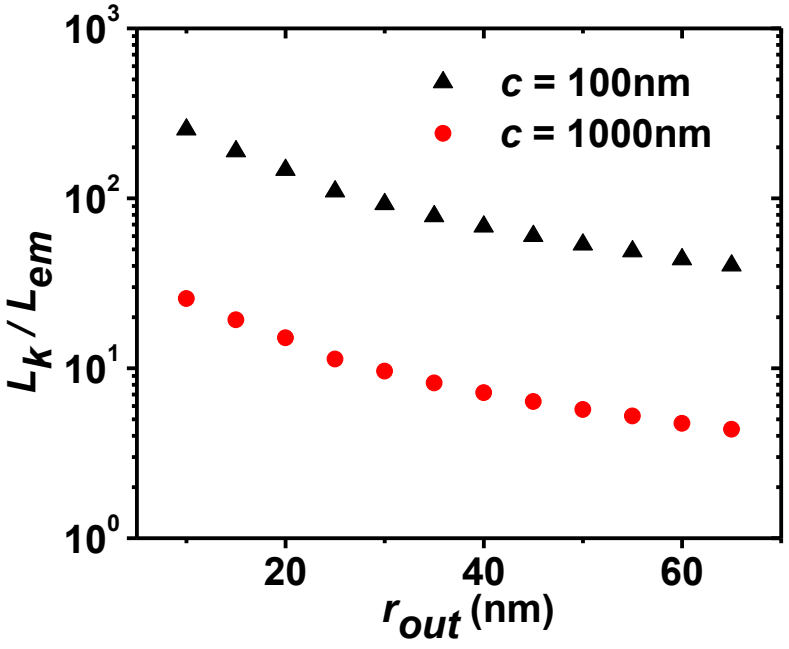

Figure 2.5: The ratio of L_k and L_{em} vs. r_{out} at c = 100nm and 1000nm

We plotted L_{net} as a function of r_{out} and c in Figure 2.4. It was then seen that the L_{net} may be tuned by orders of magnitude through varying r_{out} and c. A thinner tube (smaller r_{out}) is more effective in enhancing the inductance in that the effective flux loop area would be increased (for an equivalent I). However, the component footprint area, A (product of l_p (=$P \cdot N_t$) and width, w (=$2(r_{out}+c)$), Figure 2.1) is still diminished. The variation of L_{net} with P was found to be less significant. An enhanced $L_{M,ext}$ is particularly relevant for the proposed CCNT structure. While it has been previously found[12] that for SWNTs, $L_{M,ext}$ could be orders of magnitude lower than L_k , for CCNTs the range of variation could be smaller (Figure 2.5) due to the enhanced contribution from the *coiled* structure. In our computations, $L_{M,int}$ was found to be a small fraction (~ 1%) of the $L_{M,ext}$.

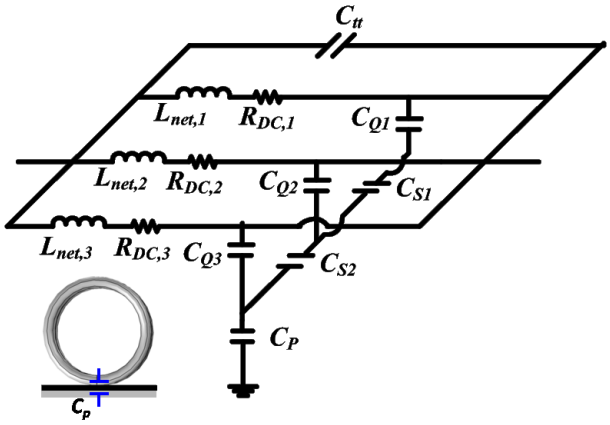

Figure 2.6: Equivalent circuit of a CCNT with all the capacitances

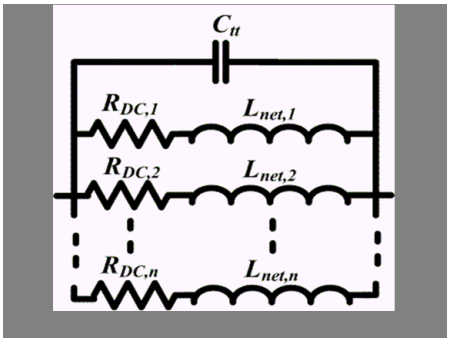

Figure 2.7: Proposed equivalent circuit of a CCNT with n shells for f_{SR} calculation

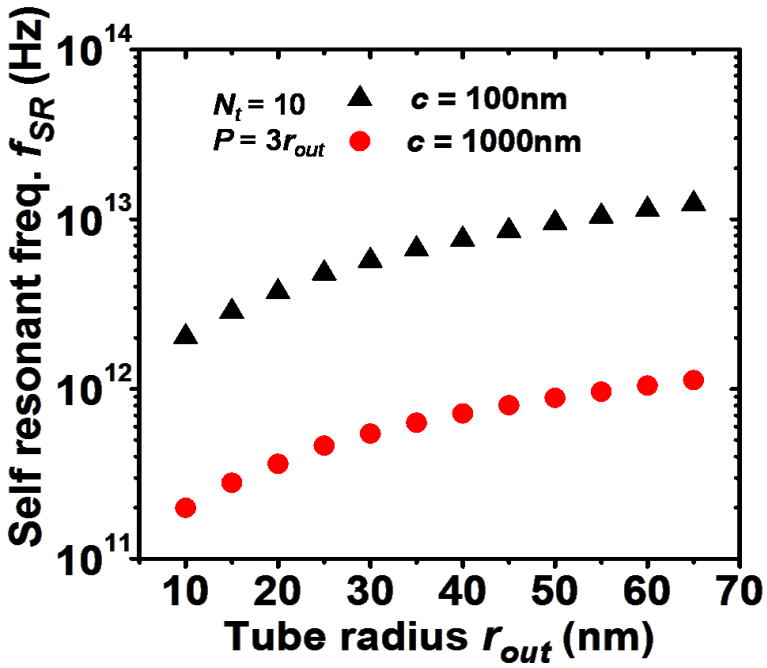

Figure 2.8: f_{SR} vs. r_{out} at c = 100nm and 1000nm

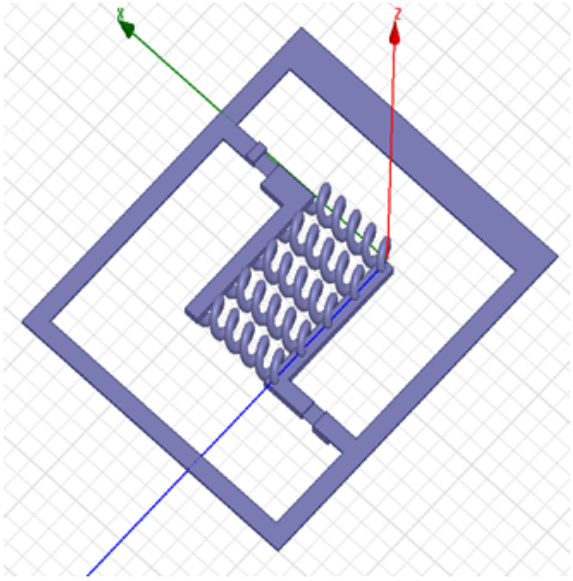

Figure 2.9: The CCNT bundle structure used in HFSS simulation with r_{out}=22nm, c = 50 nm, P =100 nm, and N_t = 5

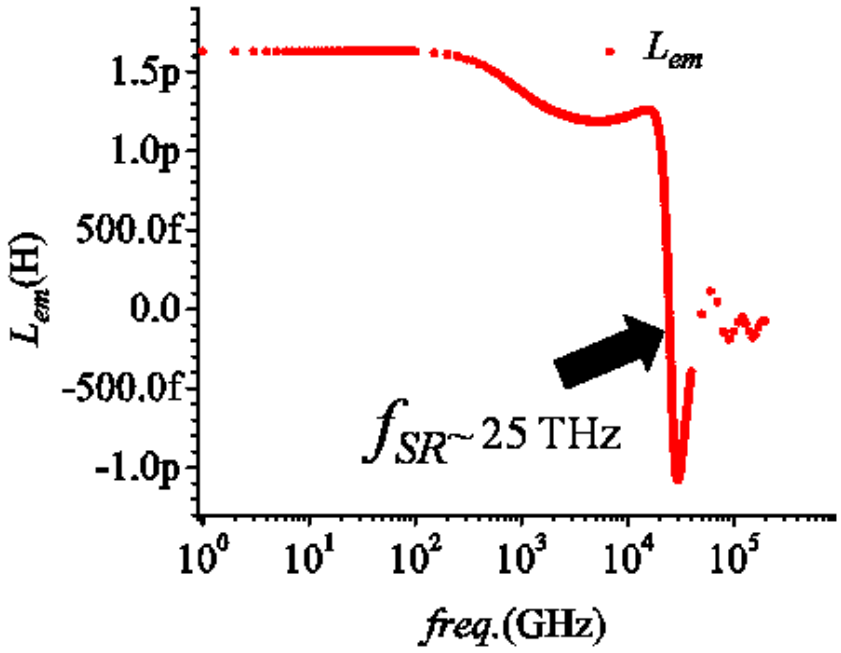

Figure 2.10: EM inductance vs *freq*. of the structure with the CCNT bundle indicating f_{SR}

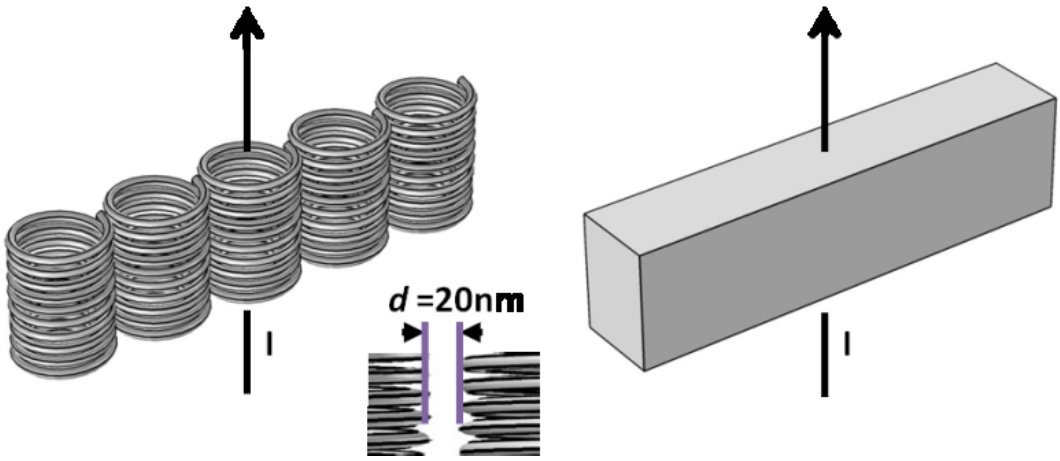

Figure 2.11: Geometry of a 5 CCNT bundle and equivalent copper block, each of the CCNT has r_{out}=10nm, c=100 nm, P=30 nm, and N_t =10, spacing between adjacent CCNT is 20nm. The direction of current flow is shown with the arrow

In addition to tunability of L_{net} and reduced A, we have also seen that other important attributes such as f_{SR} and Q could be enhanced over conventional inductors.

Presently, f_{SR} of inductors is limited to around 40 GHz[16] due to large parasitic capacitance brought about by component overlap and interaction with substrate. However, through the use of coils, f_{SR} values of the order of 10 THz may be achieved due to substantially reduced:

(i) projected/overlap area and

(ii) substrate interactions.

The equivalent circuit for obtaining f_{SR} using L_{net} and C is represented in Figure 2.7, where each shell of the CCNT was modeled as series combination of L_{net} and R_{DC}(incorporating resistance due to both quantum effects, $R_q(=\frac{h}{2e^2N_{chan}})$ and scattering, $R_s(=\frac{hl_t}{2e^2N_{chan}\lambda})$ where λ ($\sim 2000\, r_{out}$) is the electron mean free path[13]). While the individual shells of the CCNT may couple capacitively through quantum capacitance (C_q) as well as electrostatically (C_s) arising from varying voltage distributions in the shells, such capacitances do not contribute to f_{SR} due to shielding from the outer most shell (Figure 2.6). Additionally, C_p (which is in series with and typically smaller[12] than C_q) from the outer shell can be ignored due to the small projected area (Figure 2.6). The capacitance which *does* contribute to f_{SR} arises due to the interaction between adjacent turns of the coil, *i.e.,* C_{tt}. We calculated[17] the equivalent C_{tt} as 1.8 aF and $R_{DC} \sim 1.2$ kΩ (with $r_{out} = 10$ nm, $c = 100$ nm, $P = 30$ nm, and $N_t = 10$) along with L_{net}, which yields f_{SR} values in the order of 1 THz or greater (Figure 2.8). We also performed a full wave electromagnetic (EM) field simulation using high frequency structure simulator (HFSS) form Ansoft for a bundle of 5 CCNT coils (Figure 2.9) (each of which has r_{out}=22nm,

c=50 nm, P=100 nm, and N_t =5) to check the self resonant frequency (f_{SR}). The simulation results show that f_{SR} is around 25THz (Figure 2.10) when there is no parasitic capacitance from the substrate.

We compared the Q of the CCNT based inductor ensembles (Figure 2.11) (each constituent of which had a r_{out}=10nm, c =100 nm, P=30 nm, and N_t =10, with a 20 nm separation between adjacent CCNTs) with those of conventional inductors, of equivalent

(a) component footprint volume, as well as

(b) actual material volume.

Since, we propose to use parallel arrays of the CCNTs (due to a reduced resistance), five CCNTs were considered representative for comparison with prevalent inductors (which typically have widths in the range of 1-10 μm[7]). We considered both L_{net} and their mutual inductance (M_{ij})(due to the interaction of magnetic flux among neighboring CCNTs) for each CCNT in the bundle. For obtaining M_{ij} we modeled the CCNTs as solenoids with parallel axes[18]. So the overall impedance of each CCNT in the bundle will contain self impedance, $Z_{nn}(=R_{DC}+j\omega L_{net})$ and 4 mutual impedance terms for its 4 neighbors. Applying Ohm's law for all the CCNTs in the bundle we get a system of 5 linear equations:

$$\begin{bmatrix} V_1 \\ V_2 \\ V_3 \\ V_4 \\ V_5 \end{bmatrix} = \begin{bmatrix} Z_{11} & M_{12} & M_{13} & M_{14} & M_{15} \\ M_{21} & Z_{22} & M_{23} & M_{24} & M_{25} \\ M_{31} & M_{32} & Z_{33} & M_{34} & M_{35} \\ M_{41} & M_{42} & M_{43} & Z_{44} & M_{45} \\ M_{51} & M_{52} & M_{53} & M_{54} & Z_{55} \end{bmatrix} \begin{bmatrix} I_1 \\ I_2 \\ I_3 \\ I_4 \\ I_5 \end{bmatrix} \tag{2.2.6}$$

here the mutual inductance terms obtained from Grover[18] is expressed as $M_{ij}(=j\omega L_{m,ij}, i,j=1,2...5)$ and $V_1=V_2=V_3=V_4=V_5=V$, since all the CCNTs in the bundle are identical. We solved (2.2.6) for a wide range of currents (1nA to 1mA) to get V. Using V and total current, I_T $(= I_1+I_2+I_3+I_4+I_5)$ through the CCNT bundle we can compute the equivalent impedance (Z_{eff}) of the bundle, the imaginary part of $Z_{eff}(=\frac{V}{I_T}=R_{eff}+j\omega L_{eff})$ will give us the effective inductance (L_{eff}) of the bundle. This L_{eff} of the CCNT bundle was used in Table 2.1 and compared with the inductance of above described section of conventional inductor material.

Table 2.1: Comparison of L/RDC of CCNT bundle(MATLAB) and equivalent Cu block(FastHenry2)

Bundle of CCNT	**Equiv. footprint(Cu)**	**Equiv. material(Cu)**
L ~ 680pH	L ~ 0.03pH	L ~ 0.081pH
R_{DC} ~240Ω	R_{DC} ~0.02Ω	R_{DC} ~0.21Ω
L / R_{DC} ~3pH/Ω	L / R_{DC} ~1.5pH/Ω	L / R_{DC} ~0.39pH/Ω

- **Effect of Pitch on the Inductance of CCNTs**

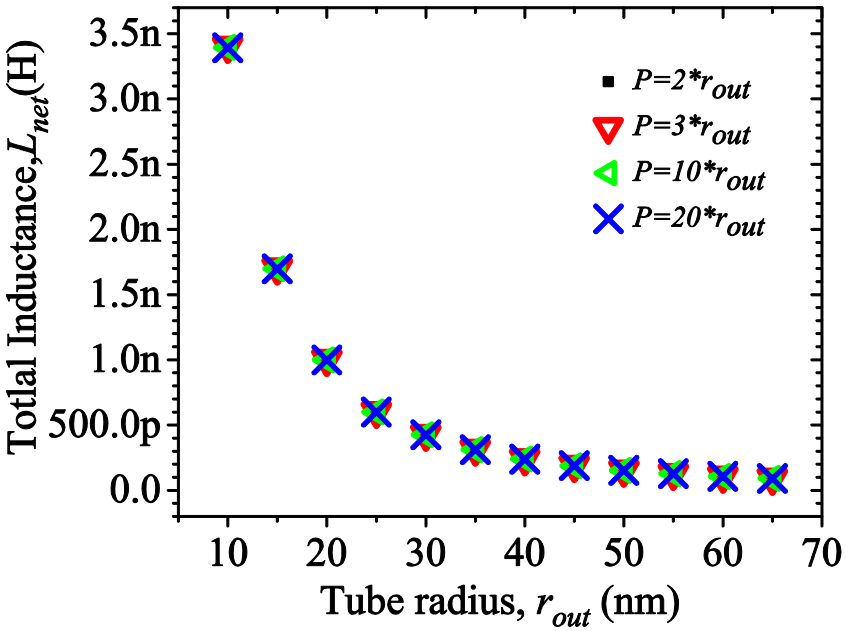

Figure 2.12: Total Inductance (L_{net}) vs Tube radius (r_{out}) with varying pitch (P). Here P is expressed as a function of r_{out}

Figure 2.12 shows the variation of L_{net} vs tube radius, r_{out} , for different P using the proposed analysis. Here we can see that L_{net} does not change significantly when we vary P, so squeezing and unsqueezing the CCNTs will have negligible effect on L_{net}.

2.3 Experimental Details

- Synthesis Procedure

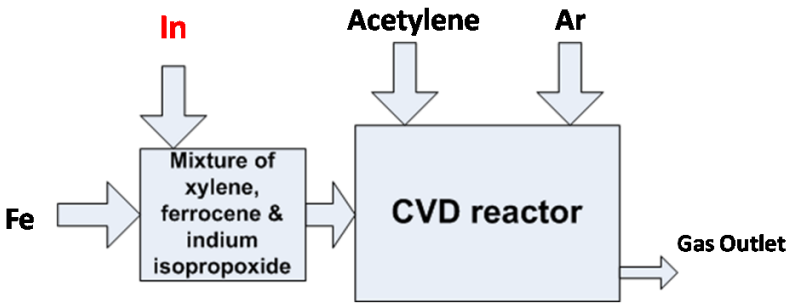

Figure 2.13: Simplified block diagram of CCNT synthesis

A two-stage CVD reactor comprising of liquid and gas injectors was used for preparing CCNTs on bare quartz substrates (Figure 2.13). Xylene and acetylene served as the carbon source. Indium isopropoxide was dissolved in the xylene-ferrocene mixture which was continuously injected into the CVD reaction tube (~700 ^{o}C) at the rate of 1ml/hr. The atomic concentration of Fe in the xylene-ferrocene mixture was held between 0.75 -1 atomic %, and the relative concentration of Indium isopropoxide was varied systematically to yield catalyst particles with varying catalysts compositions R=In/(In+Fe). Acetylene at the flow rate of 50 sccm and argon at the flow rate of 800 sccm were fed into the system during the synthesis. After 1 hour reaction, the syringe pump and acetylene injection were shut off and the CVD reactor was allowed to cool to room temperature under flowing argon atmosphere. Various parameters, such as the reactor temperature, gas flow rate, concentration of iron, and indium were adjusted to optimize the synthesis condition. Scanning electron microscopy (SEM) (Haitachi S-4700, 20 KV) and transmission electron microscopy (TEM) (Hitachi HD-2000, 200 KV) were employed to explore the structure and morphology of the as-grown HCNTs.

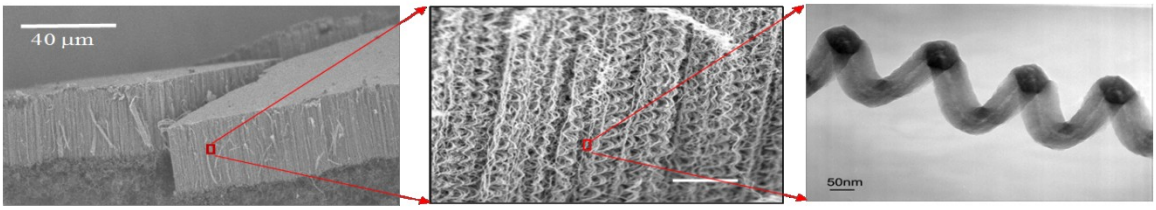

Figure 2.14: SEM images of CCNTs

We find that the growth of CCNTs is favored when R is ~65%. Figure 2.14 shows a typical SEM image of an as-grown CCNTs film that was peeled from the quartz substrate. High purity CCNTs are densely packed and oriented normal to the surface of substrate. The high degree of orientation can be appreciated from the middle section of the CCNTs array as seen in Figure 2.14.

- Sample Preparation

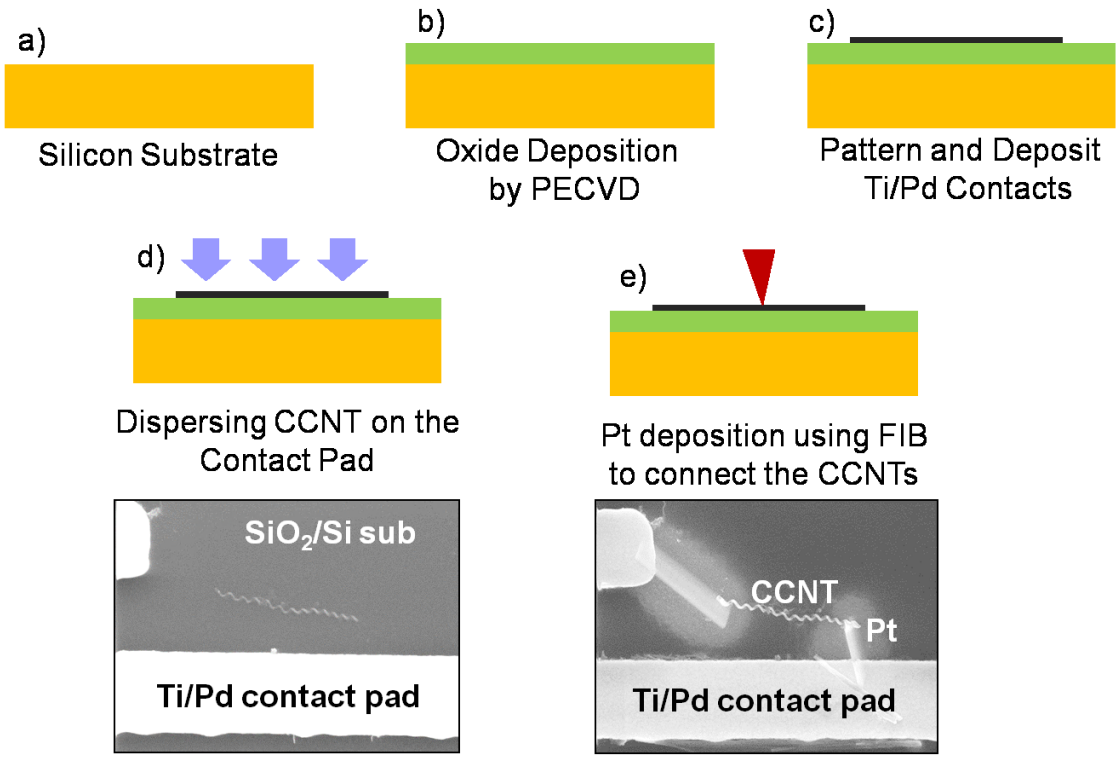

Figure 2.15: Fabrication steps for sample preparation

After fabricating CCNTs we need to create contacts on them for characterization. To create contact pads we start with a Si substrate and deposit an insulating layer on them and then pattern and deposit Ti/Pd contact pads, then we disperse the CCNT containing liquid on the substrate, after this the SEM image looks like this, then we connect the CCNT with the contact fingers with FIB based Pt deposition. In this way we package our CCNTs for characterization. All the fabrication steps are illustrated in Figure 2.15.

- Measurements

After preparing the samples (Figure 2.16), they were measured using Agilent B1500A semiconductor parameter analyzer coupled to a commercial probe station. Four terminal pair (4TP) configuration connection method was used to reduce the parasitic

(Figure 2.17). In order to estimate the contact resistance, a FIB deposited Pt metal line was also measured. As we can see from Figure 2.18 that the measured CCNT has a resistance of ~10KΩ, where as the theoretical computation suggest only ~4Ω. Also the resistance of the Pt line is ~1KΩ, where the computation predicts ~9Ω. Also the phase shift indicates purely resistive behavior.

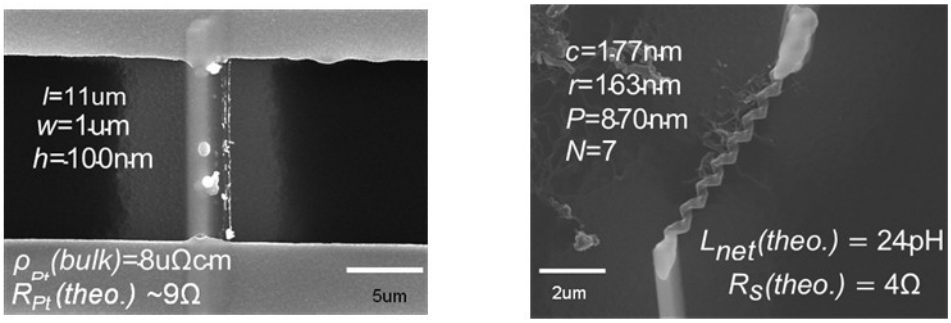

Figure 2.16: Measured Pt line and CCNT with theoretical estimation of resistance

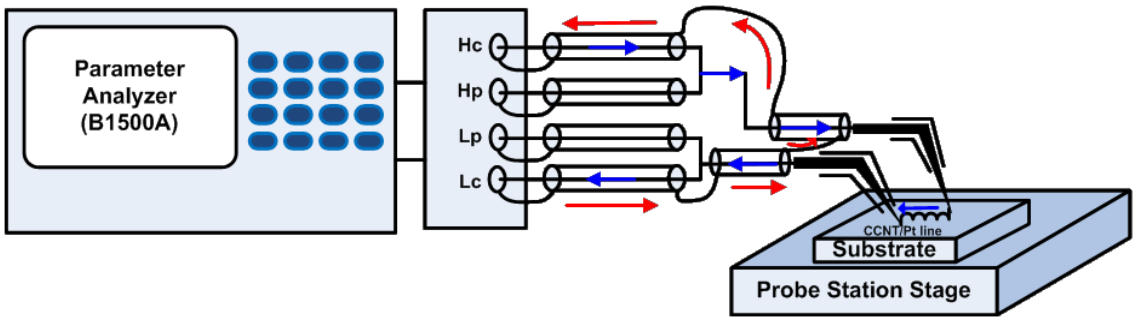

Figure 2.17: Measurement setup used for CCNTs and Pt metal line

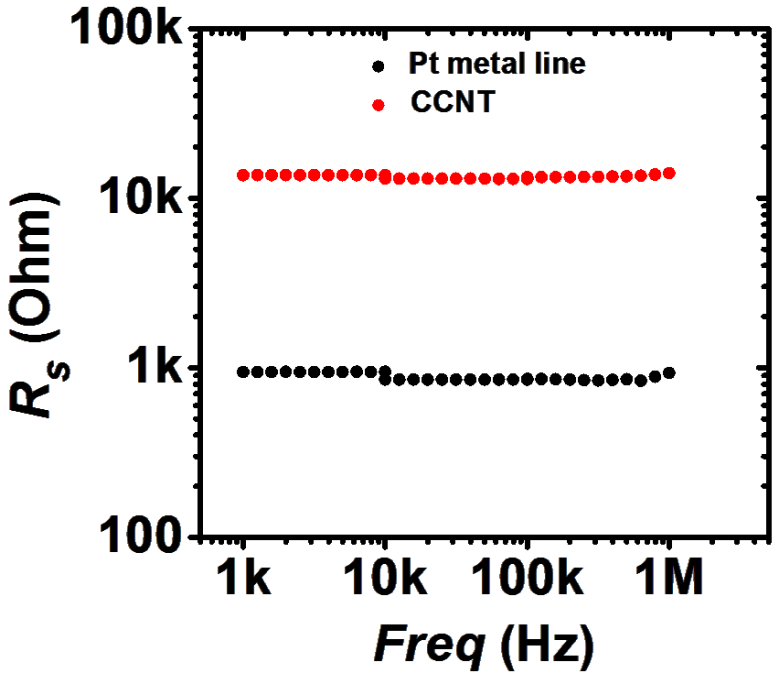

Figure 2.18: R_s vs *freq.* of the Pt line and the CCNT

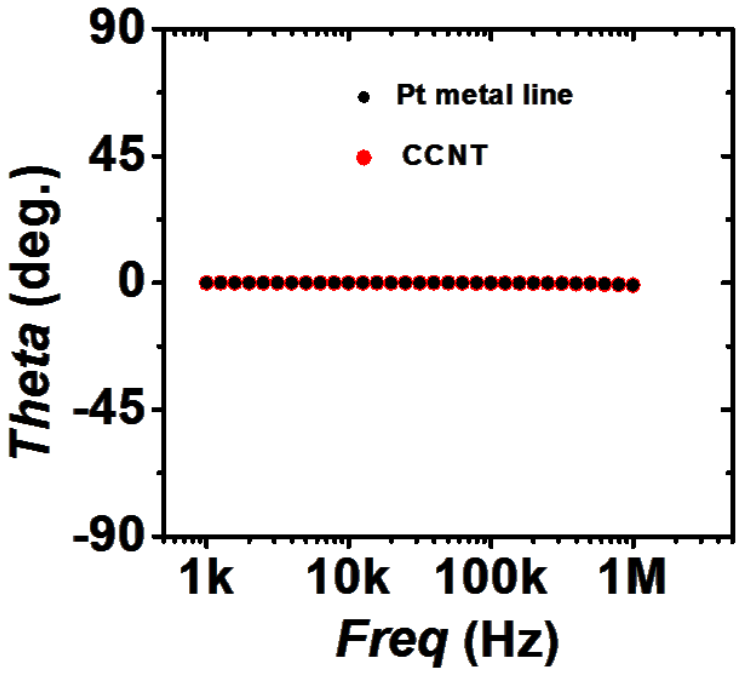

Figure 2.19: Phase shift (Theta) vs. freq. of the CCNT and Pt metal line

This experimental measurement suggested that the impedance of the CCNTs are dominated by their orders of magnitude higher contact resistance. Also the FIB deposited metal lines, which were used as the contacts, have at least 100 times higher resistance than their bulk counterpart which is a major source of the high contact resistance. So in order to truly characterize the impedance of the CCNTs we need to significantly reduce their contact resistance which warrants a detailed investigation of the resistivity of the FIB deposited metal lines.

2.4 Conclusion

In summary, we have suggested, based on computations of the constituent electrical characteristics, that rationally synthesized CCNTs could be used as inductor elements. FIB deposited metal deposition process needs to be optimized for reducing the contact resistance of the CCNTs. Low contact resistance(~few Ωs) are extremely critical for the experimental verification of the simulated inductance.

This chapter, in part, is a reprint of material as it appears in the following publications: H M Faraby, A M Rao, and P R Bandaru, “Modeling high energy density electrical inductors operating at Thz frequencies based on coiled carbon nanotubes”, *IEEE-Electron Device Letters, Vol. 34, Issue 6.*H Faraby and P R Bandaru, “High Energy Density, High Operating Frequency and Energy Efficient On-Chip Inductors based on Coiled Carbon Nanotubes (CCNTs).”*MRS Online Proc Libr. 2013;1551*. The dissertation author was the primary investigator and author of this material.

Chapter 3 Focused Ion Beam Deposited Metals

This chapter will discuss the effect of elemental concentration on the resistivity of FIB deposited Pt and W metal lines. It will also report how the resistivity and the Ga concentration varies with different beam parameters. Finally it will provide a mathematical model to estimate the resistivity of the metal lines from the Ga concentration only.

3.1 Introduction

FIB based techniques are of wide use in the semiconductor industry, and play a critical role in applications including, *e.g.,* metal deposition induced repair of integrated circuits[19], cross section imaging of micro-fabricated devices[20], electron microscopy (EM) sample preparation[21], *etc*. FIB induced metal deposition has also been extensively used in electrical connection and concomitant measurements of nanostructures such as nano-tubes/-wires[22,23,24], quantum dots[25], and related devices[26]. Typically, for metal deposition Ga^+ constituted ion beams serve to decompose the metallo-organic (MO) precursors – which serve as the source for the metal.

However, a major issue in FIB induced metal deposition is the sub-optimal electrical resistance of the deposited metals (*e.g.,* in the case of platinum[27,28,29], gold[30], coppper[31], cobalt[32], and tungsten[33]), where electrical resistivity values have been reported to be orders of magnitude higher than that of the bulk metal. While it has been widely perceived[27-29,33] that contamination from the carbon of the precursors decreases the

resistivity, we will show, based on extensive experimental investigations, that the resistance seems to be controlled by the implanted Ga^+ - with the metal from the MOs playing a negligible role.

The FIB metal deposition process involves heating (typically to ~ 50 ^oC) the relevant MO precursor in a gas reservoir adjacent to the EM chamber, subsequent to which MO vapor is controllably passed, through a gas nozzle, into the vacuum chamber. It is thought[34] that the vapor molecules adsorb onto the substrate, and are then decomposed through interaction with the ion beam. The decomposition of the MO precursors should result in metal deposition, the thickness of which should be proportional to the MO-ion beam interaction time, while the residual volatile organics are concomitantly removed through vacuum pumping. A few prior reports[35,36] have investigated the relationship of different beam parameters on the growth rate and resistivity of deposited metal lines. It was found[35] that the resistivity can be varied by orders of magnitude by varying the deposition parameters and the presence of Ga^+ has an positive[36] impact in reducing the resistivity of electron beam deposited Pt metal lines. While it was also indicated[22] that a metal-insulator transition as a function of nanowire diameter occurs in FIB deposited Pt-C nanowires (with diameters in the range of 70-150 nm), the relationship of the resistivity variation with Ga^+ concentration was not mentioned.

3.2 Experimental Details

We focus, on the electrical resistance of tungsten (W) and platinum (Pt) metal lines deposited in commercial FIB/SEM systems using Trimethyl (methylcycopentadienyl) platinum: $C_9H_{16}Pt$, and tungsten hexacarbonyl: $W(CO)_6$, as the respective MO precursor gases. During the deposition, the ion beam accelerating voltage was fixed at 30 kV, *e.g.,* to minimize the contribution of the secondary electrons[37]. Four commonly used metal deposition parameters were investigated, *viz.,*

(i) *beam current* - which defines the total Ga^+ charge/unit time (in the range of 80 pA to 2.5 nA for Pt and 80 pA to 9.3 nA for W)

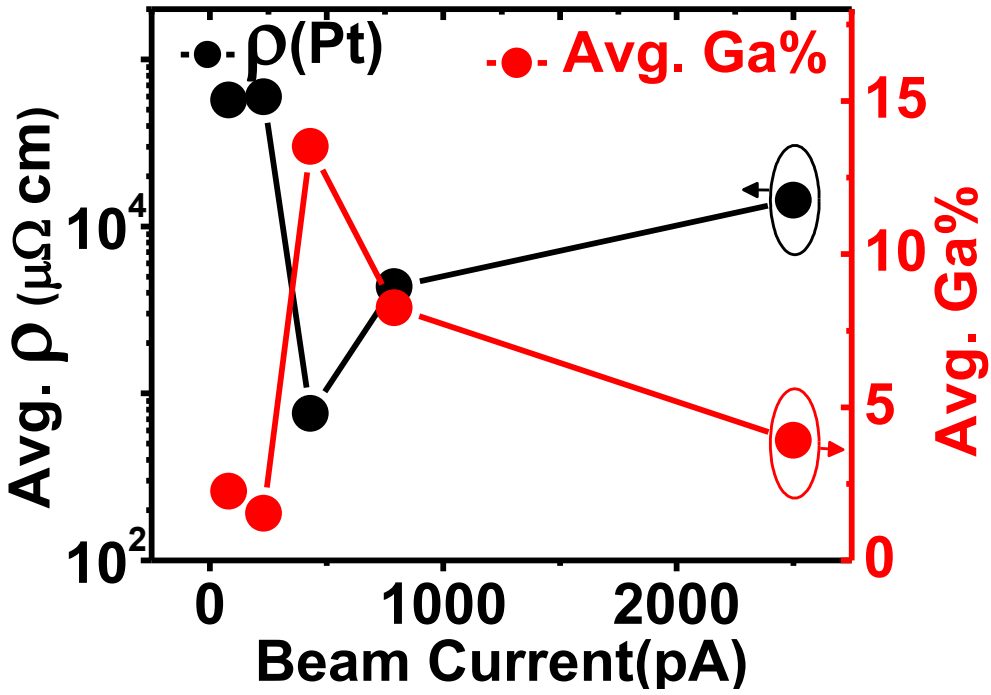

Figure 3.1: Avg. ρ and Ga% vs beam current for Pt

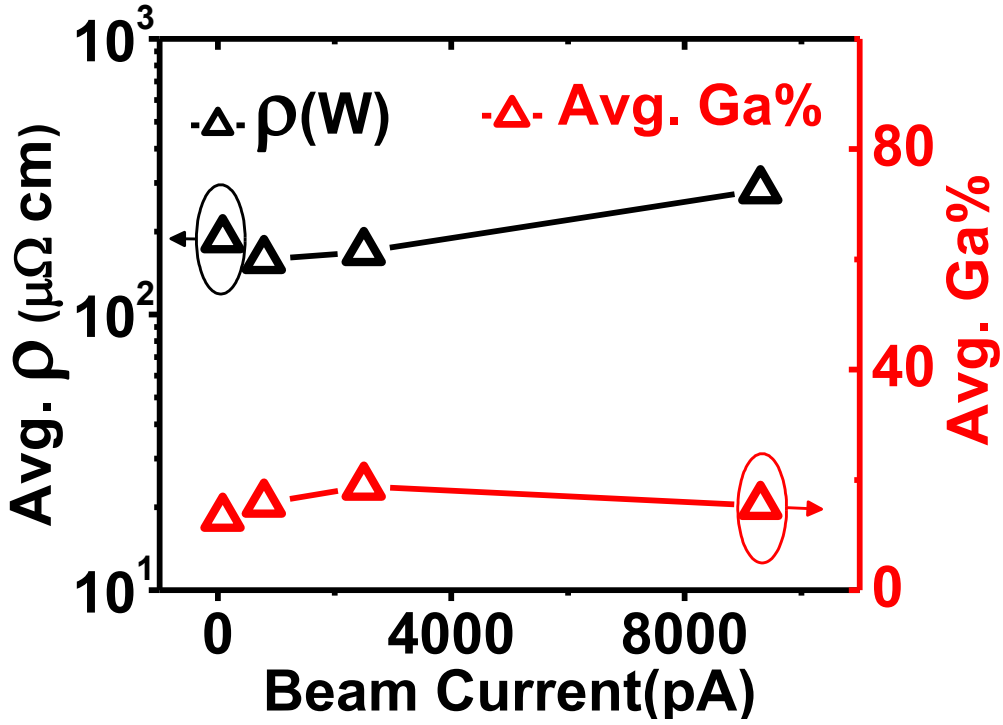

Figure 3.2: Avg. ρ and Ga% vs beam current for W

In Figure 3.1and Figure 3.2 we plotted the average ρ and average Ga concentration with respect to beam current for Pt and W respectively. We can see that for both Pt and W whenever there is an increase or decrease is Ga concentration there is a corresponding decrease or increase in resistivity (ρ) which indicates a direct dependence of Ga concentration with resistivity. Since the resistivity variation is from 100 μΩ-cm to 400 μΩ-cm we should get similar dependence with respect to C and W concentrations also.

(ii) *percentage of overlap* between adjacent beam spots (in the range of 0% to -150%), illustrated in Figure 3.3. The percentage overlap is based on the theoretical spot size of the ion beam based on the aperture selected. A negative overlap number

positions the beam spot locations such that there are a gap in between the dwell points of the ion beam. A positive overlap number indicates that the spot locations will have intersecting areas during the patterning activity. Figure 3.3 shows a simple example of the beam spacing for the range and midpoint of the beam overlap conditions. The image on the left shows an overlap of 0%, meaning no gap between adjacent beam spots the right one shows an overlap of -150%. The experimental range investigated was purposely skewed toward negative values because gas enhanced recipes such as deposition are known to depend upon other effects such as beam tails and secondary electrons (SE) to drive the subsequent chemical reactions.

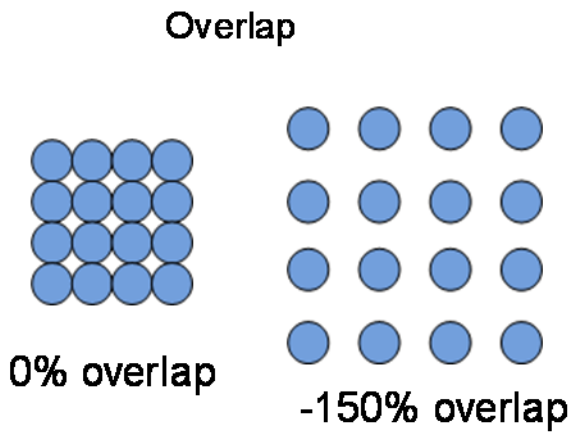

Figure 3.3: Illustration of the concept of overlap%

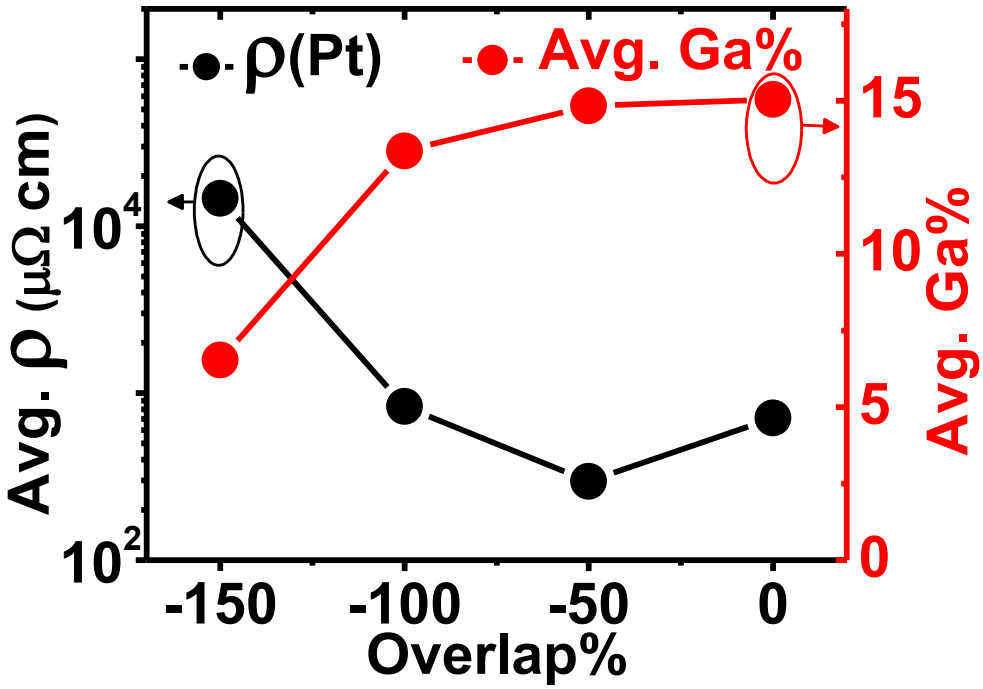

Figure 3.4: Avg. ρ and Ga% vs overlap% for Pt

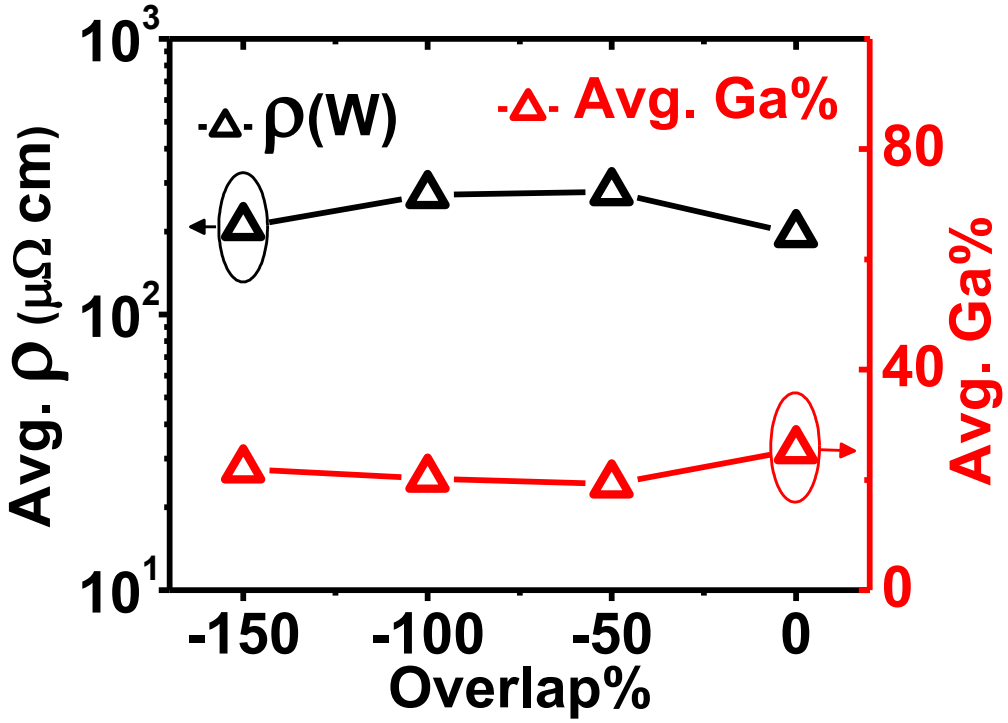

Figure 3.5: Avg. ρ and Ga% vs overlap% for W

In Figure 3.4 and Figure 3.5 we plot how the resistivity (ρ) and the Ga concentration changes with overlap % for Pt and W respectively. Here we also see the same relation of ρ and Ga concentration as we have seen for beam current. We also notice that similar to beam current the ρ and Ga concentration of W doesn't change much with overlap%.

(iii) *defocus* – a measure of the ion beam spread (in the range of 0 μm to 150 μm), with respect to the sample surface as a reference, this value offsets the final focus position during patterning and results in larger beam spot size parameter by automatically controlling the lens 2 voltage (focus) on the ion column. This results in spreading the ion beam current across a larger area and less collimated beam during the

depositions. The defocus value is only active during patterning and returns the lens value to optimal focus when the pattern recipe is complete. The concept of defocus is illustrated in Figure 3.6.

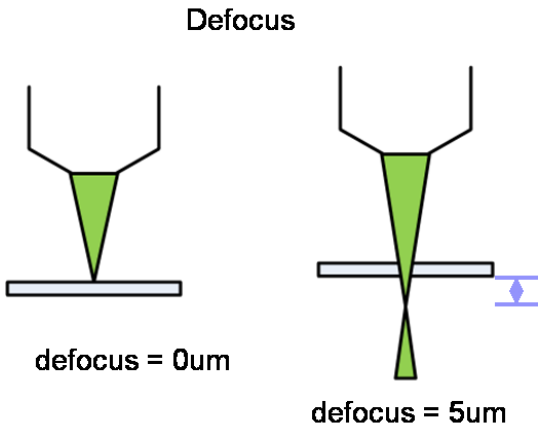

Figure 3.6: Illustration of the parameter defocus

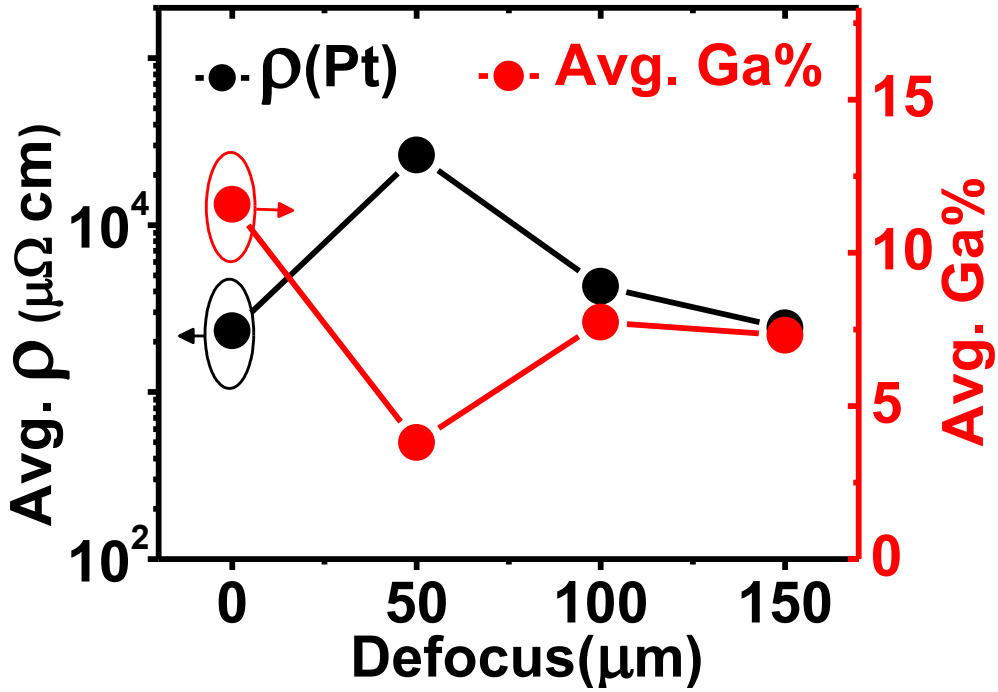

Figure 3.7: Avg. ρ and Ga% vs defocus for Pt

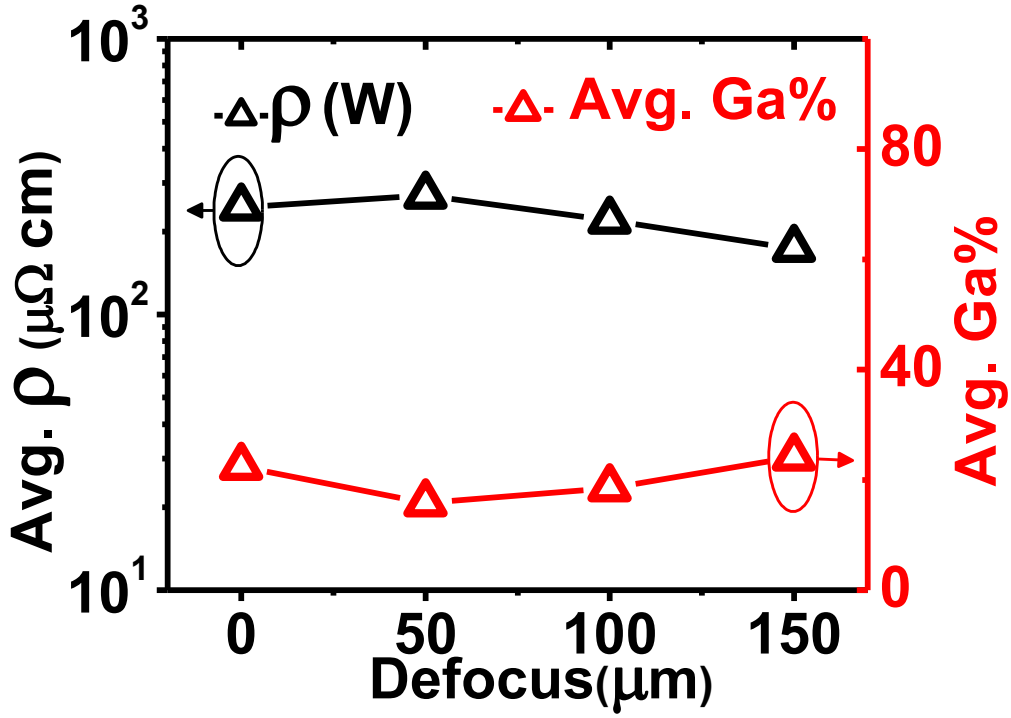

Figure 3.8: Avg. ρ and Ga% vs defocus for W

In Figure 3.7 and Figure 3.8 the resistivity ρ and Ga concentration is plotted with respect to defocus. We see the same trend and we have seen for beam current and overlap.

(iv) *temperature* of the gas injection system (GIS), which regulates the MO gas pressure (in the range of 42 ^{o}C to 54 ^{o}C for Pt and 41 ^{o}C to 62 ^{o}C for W) in the vacuum chamber. The GIS temperature controls the flow of the precursor gas in the vacuum chamber. By controlling the GIS temperature we regulate the volume of gas available for interaction with the high energy ion beam. The volume of gas available for ion beam interaction can greatly control the chemical composition of the deposited material as if the gas volume is too much compared to Ga ion then there will a significant

amount of un-decomposed precursor gas elements present in the deposition which will result in a higher resistivity deposition and if the gas volume is too little then a lot of Ga ions will be deposited which will make the resistivity relatively lower as we can see from Figure 3.9 and Figure 3.10, also there is the risk of running in a gas depleted regime, where there isn't enough precursor gas available to deposit and the Ga ion beam sputters the substrate.

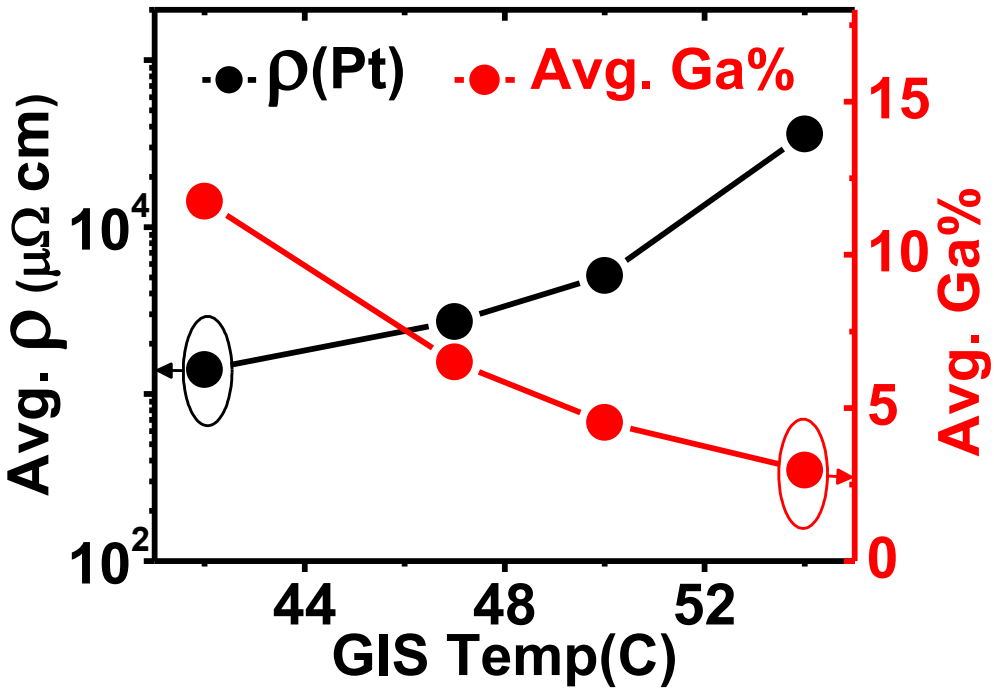

Figure 3.9: Avg. ρ and Ga% vs GIS Temp. for Pt

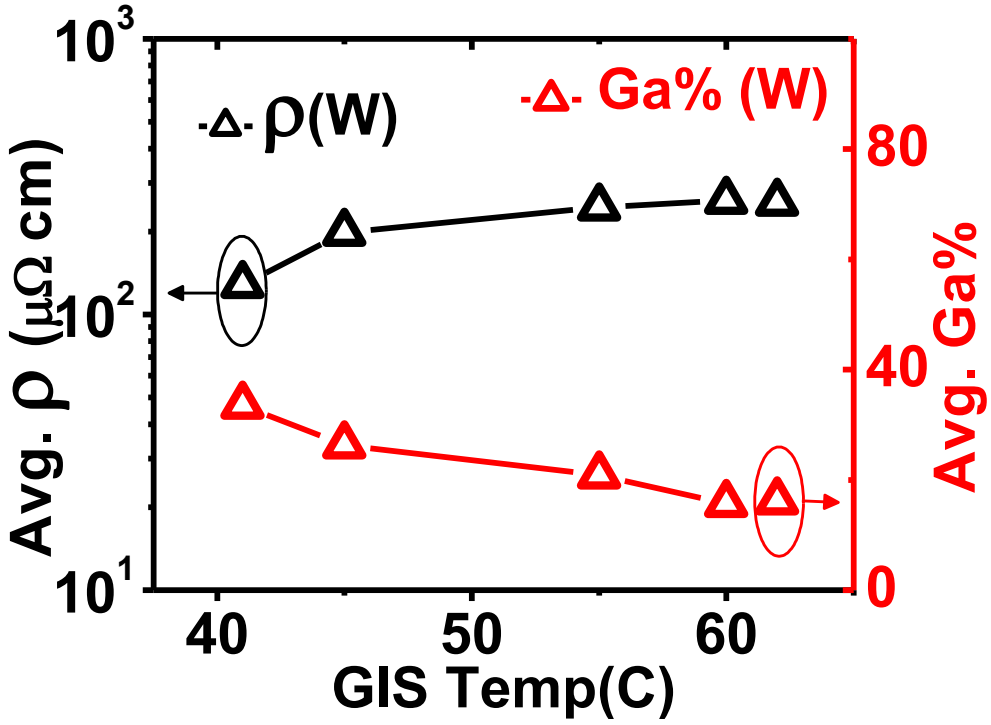

Figure 3.10: Avg. ρ and Ga% vs GIS Temp. for W

From the previous plots we can predict a clear relation of decreasing resistivity with increasing Ga concentration for both Pt and W. The plots also indicate that the resistivity does not depend on either beam controlling parameters or gas flow controlling parameters; rather it depends on the elements that are present in the deposition.

Now we would like to discuss how we obtained the concentrations of the constituent elements which were present in the deposition and used in the above mentioned plots.

Subsequent to depositing the W and Pt metal lines, the chemical composition of all the constituent elements was quantitatively analyzed through the standard practices of energy dispersive spectroscopy[37] (EDS). When a sample is scanned with a beam of high

energy electrons, characteristics X ray photons are generated along with Bremsstrahlung. The energy of those characteristic X-rays belong to the emission energies of the chemical elements contained in the sample, those energies are independent of the chemical bonding state of the affected atoms. In the resulting energy dispersive spectrum the characteristic X-rays correspond to visible peaks. Identifying these peaks yields information about the elements that are present in the sample. Bremsstrahlung (deceleration radiation) is generated by deceleration of high-energy electrons in the electric field of an atomic nucleus. Thereby the electron looses a substantial amount of energy which was supposed to be released in form of an X-ray. Since any value of energy loss - from zero to the full electron energy – is possible, the Bremsstrahlung quanta statistically form a continuous spectrum background. Using those background and peak intensities, quantitative data about the sample composition is derived by an extensive mathematical process often referred as P/B ZAF matrix correction. Here P/B is the ratio of peak to background intensities of the generated X rays and Z, A and F represents atomic number factor, absorption factor and fluorescence factor respectively.

The Z-factor accounts for the ratio of total counts to the number of incident electrons; the A-factor is the effect of self-absorption of the characteristics X rays by the elements in the sample and the F-factor accounts for the fluorescence enhancement, all these are non-ideal effects which needs to be corrected for accurate quantitative analysis. This method is considered as a true standard less and self calibrating method as it does not require measured intensities of characteristic X rays of standard materials for quantitative analysis. The detailed mathematical process is published elsewhere[38]. In this

way the chemical elements and their respective atomic percentage of the FIB deposited metal lines were obtained.

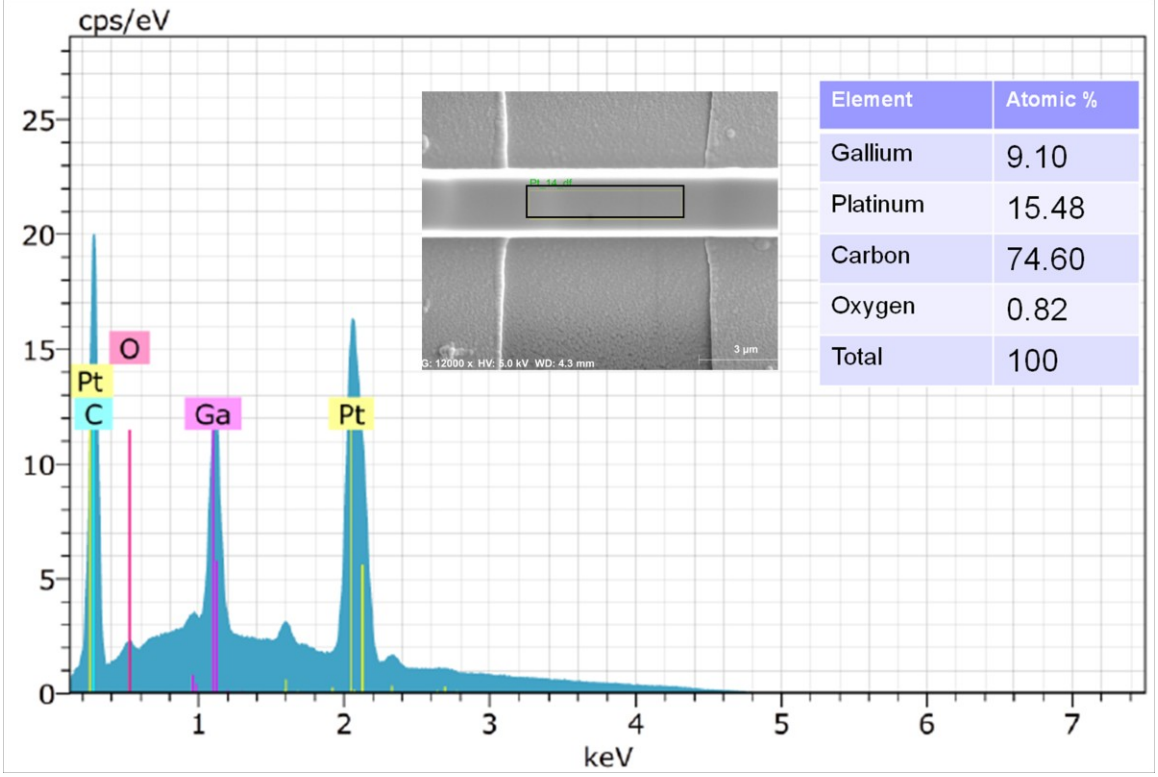

Figure 3.11: Example of an measured EDS Spectrum

Figure 3.11 shows an measured EDS spectrum. The diagram on the inset is the SEM image of the deposited metal and the black box indicates the area on which EDS analysis was performed, and the table on the inset shows the atomic concentration of the elements calculated from the spectrum.

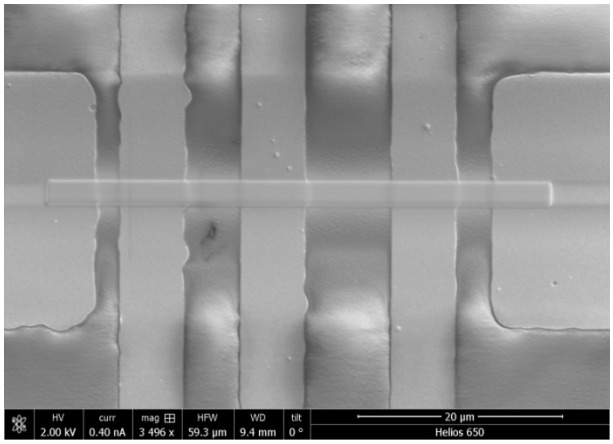

Figure 3.12: FIB deposited metal line on the contact pads

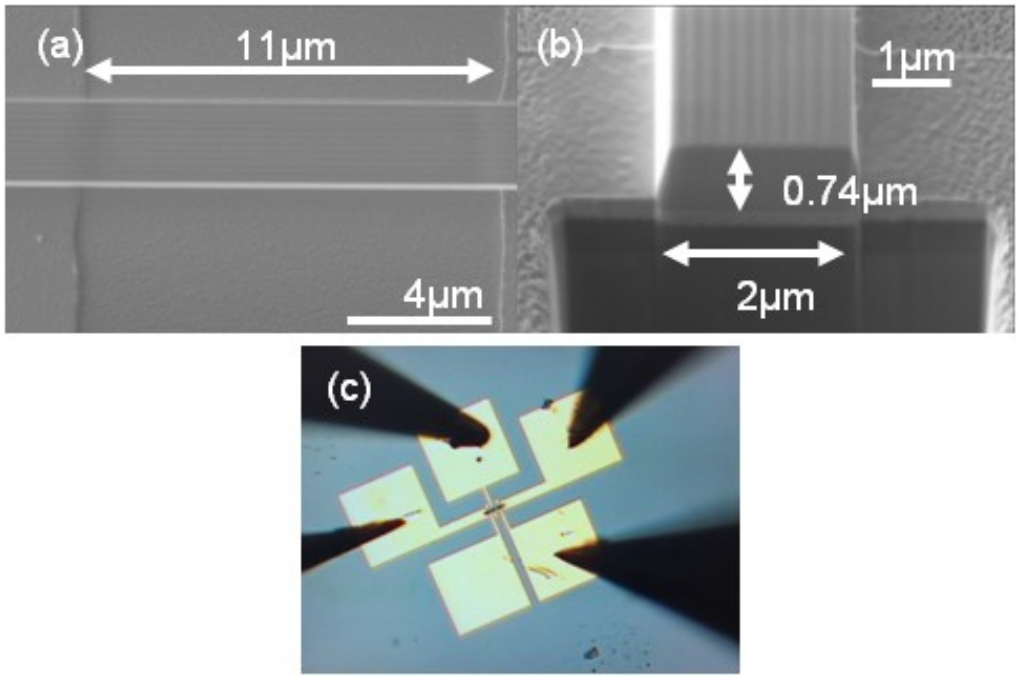

Figure 3.13: Scanning Electron Microscopy (SEM) images of the (a) length (*l*), along with the (b) width (*w*) and height (*h*) of FIB deposited metal lines. (c) Optical image of the four-probe measurement of the electrical resistance on the FIB metal lines

The deposited metal lines were contacted through Ti/Pd pads (patterned on plasma-enhanced chemical vapor deposited SiO_2 coated Si substrate) for electrical

measurements (Figure 3.12). The electrical resistivity (ρ) of the material was determined through four-probe measurements: Figure 3.13(c), of the resistance (R) of the deposited metal lines (using a HP 34401A multimeter and a commercial probe station). The length (l) – Figure 3.13(a), along with the width (w) and the height (h) – Figure 3.13(b), of the metal lines were estimated from EM imaging and FIB cross sectioning.

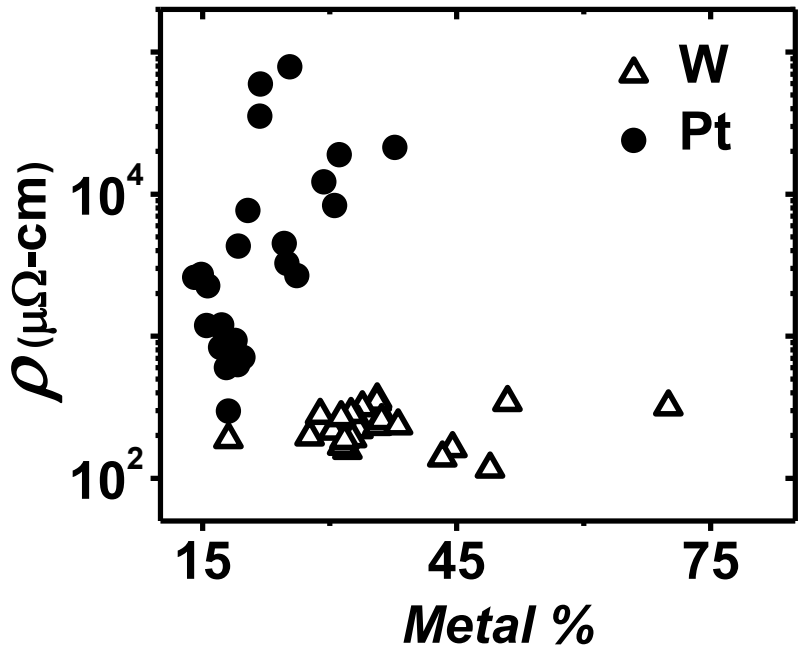

Figure 3.14: The variation of the electrical resistivity (ρ) with metal (M)(Pt or W)

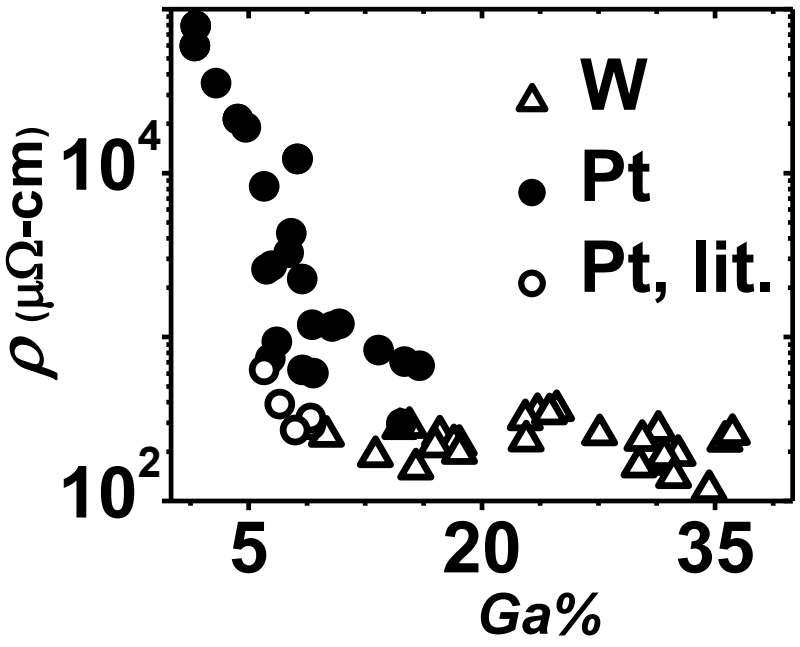

Figure 3.15: The variation of the electrical resistivity (ρ) with gallium (Ga),

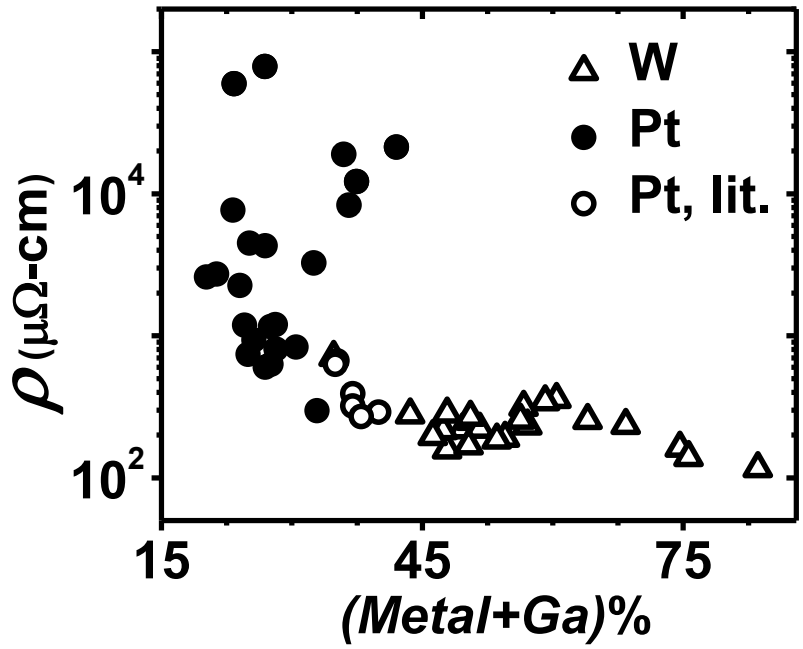

Figure 3.16: The variation of the electrical resistivity (ρ) with conductors (M+Ga)

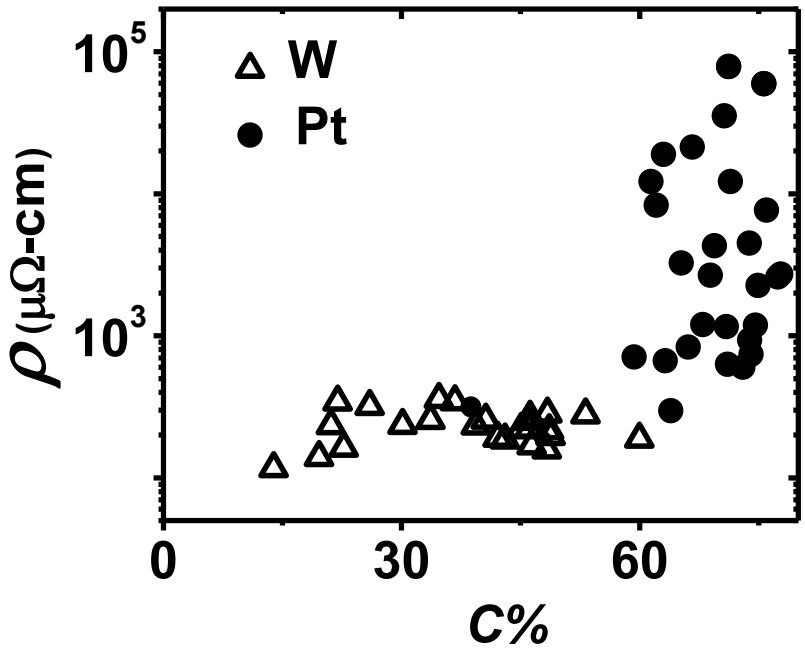

Figure 3.17: The variation of the electrical resistivity (ρ) with carbon (C)

We plot the estimated resistivity, $\rho(=Rwh/l)$ with respect to M (*i.e.,* W or Pt) and Ga atomic % in Figure 3.14 and Figure 3.15 respectively. Generally, the ρ relates to the decomposition product of the MO precursor while EDS (used for determining the atomic %) identifies elements independent of their chemical bonding state. Figure 3.14 does not seem to indicate any clear correlation () of ρ with atomic % of M. For Pt (with bulk resistivity ~10.6 μΩ-cm) metal lines, the ρ was noted to be in the range of 10^2 -10^5 μΩ-cm, with a metal concentration (as determined through EDS) in the range of 20% to 40%. For W metal (with concentrations between 30-40%) lines, the ρ was found to be smaller[29,39] - in the range of 100-400 μΩ-cm , while still larger than that of the bulk W (~5.5 μΩ-cm). However, a clear correlation of decreasing ρ, indicating increasingly

metallic characteristics, with increasing Ga concentration was observed and is shown in Figure 3.15. The Ga content was kept adequately low to avoid sputtering effects associated with larger fluences[40] at higher atomic % Ga. The variation of the ρ with (M+Ga) atomic % is indicated in Figure 3.16, showing trends similar to Figure 3.15 . In Figure 3.16 , previously published[41] data have been superposed. While there seem to be some deviatory data in Figure 3.16, their corresponding Ga concentrations – as in Figure 3.15 - still conform to the trend of decreasing resistivity, indicating that Ga is the dominant factor in determining the electrical resistivity of the FIB deposited metal lines. In Figure 3.17 we plot the variation of ρ with C atomic %. Here we see as the C atomic % increases, ρ decreases indication carbon role as an insulating material, the spread in resistivity was wider than the metal(M) and gallium(Ga).

3.3 Theoretical Modeling

In order to understand the percolative behavior of the electrical resistivity of the FIB deposited metal,, we theoretically calculated their electrical resistivity using the concept of effective medium theory (EMT). It relates to methodical modeling that outlines the macroscopic properties of composite materials. They are derived from averaging the pristine values of the properties of the constituents that directly make up the composite material.

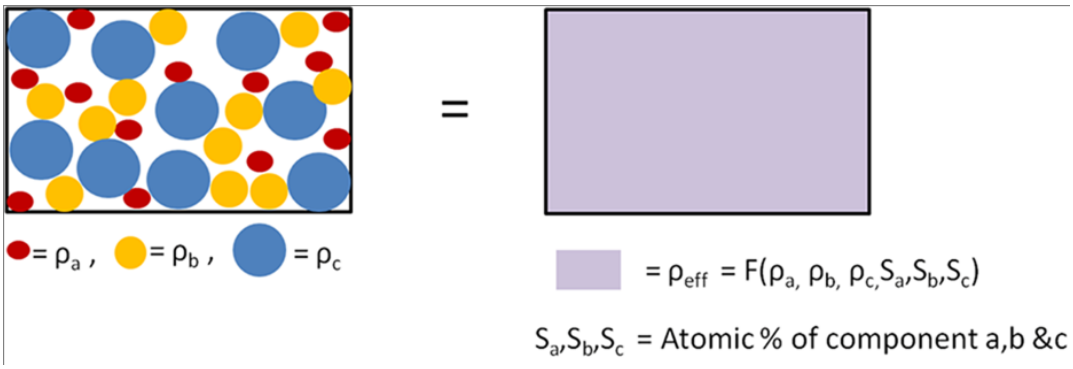

Figure 3.18: An intuitive explanation of the Effective Media Theory (EMT)

Many theories have been developed which can describe useful properties of the composite material as a whole. In this case, the theoretical resistivity of the MO deposited metal-Ga-C composite was estimated through McLachlan's[42,43,44] general effective medium (GEM) based formulations[45], developed as a generalization and expansion of Bruggeman's symmetric and asymmetric media theories for binary mixtures. We assumed that the mixture was constituted from two components - a low resistivity (ρ_{lo}) component (mainly from Ga with a resistivity of 27 μΩ-cm[46]) and a high resistivity (ρ_{hi}) component from C, un-decomposed MO precursor, *etc*. and that the variation observed in Figure 3.15 corresponded to a percolative transition, where increasing Ga through the FIB deposited metal line increased the overall electrical conductivity. While the symmetric theory was based on a random mixture of distinct spherical constituents, which completely fill the composite media (of resistivity: ρ_m), the asymmetric theory assumes concentrically coated constituents. The following form of the GEM equation was employed:

$$\frac{\varphi\left[(\rho_m)^{\frac{1}{t}}-(\rho_{lo})^{\frac{1}{t}}\right]}{(\rho_m)^{\frac{1}{t}}+\left[\frac{1-\varphi_c}{\varphi_c}\right](\rho_{lo})^{\frac{1}{t}}}+\frac{(1-\varphi)\left[(\rho_m)^{\frac{1}{t}}-(\rho_{hi})^{\frac{1}{t}}\right]}{(\rho_m)^{\frac{1}{t}}+\left[\frac{1-\varphi_c}{\varphi_c}\right](\rho_{hi})^{\frac{1}{t}}}=0 \qquad (3.3.1)$$

In Eqn. (3.3.1), $\varphi$is the atomic percentage of the low resistivity component (with $\varphi_c$being a critical atomic percentage of Ga at which a percolation path is formed through the medium) and *t* is a critical exponent. Eqn. (3.3.1) reduces to Bruggeman's symmetric and asymmetric media equations in the appropriate limits of the resistivity and shape of the components [43], and can also be viewed as an electrical conductivity/resistivity percolation equation[43]. For example, when $\rho_{lo} \rightarrow 0$, Eqn. (3.3.1) reduces to:

$$\rho_m = \rho_{hi}\left(1-\frac{\varphi}{\varphi_c}\right)^t \qquad (3.3.2)$$

Alternately, with $\rho_{hi} \rightarrow \infty$, Eqn. (3.3.1) yields:

$$\rho_m = \rho_{lo}\left(1-\frac{1-\varphi}{1-\varphi_c}\right)^{-t} \qquad (3.3.3)$$

Eqn. (3.3.1) can be considered as a matched asymptotic expression[42] between Eqns. (3.3.2) and (3.3.3) with φ_c being the matching asymptote. The $\rho_{lo}$was chosen as 27μΩ-cm which is the resistivity of liquid metal Ga[46]. The ρ_{hi} was chosen to be 10^5 μΩ-cm which is obtained by extrapolating the experimental data (Figure 3.15) to 0% Ga concentration. Other two fitting parameters *t* and φ_c are fitted to 1.3 and 0.05 respectively. In order to verify the range of φ_c , it was calculated using both Eqn. (3.3.2)

(φ_{c2}) and Eqn. (3.3.3) (φ_{c3}) where ρ_m and φ was obtained from the experimental data of Figure 3.15 and aforementioned values of t, ρ_{lo} and ρ_{hi} were used. It was observed that the matching $\varphi_c(=\varphi_{c2}=\varphi_{c3})$ resides between 0.048 and 0.07 as $\Delta\varphi_c(=|\varphi_{c2}-\varphi_{c3}|)$ was minimum (~0.02). Using these parameters Eqn. (3.3.1) was solved numerically with MATLAB for ρ_m and plotted with the experimental data in Figure 3.19.

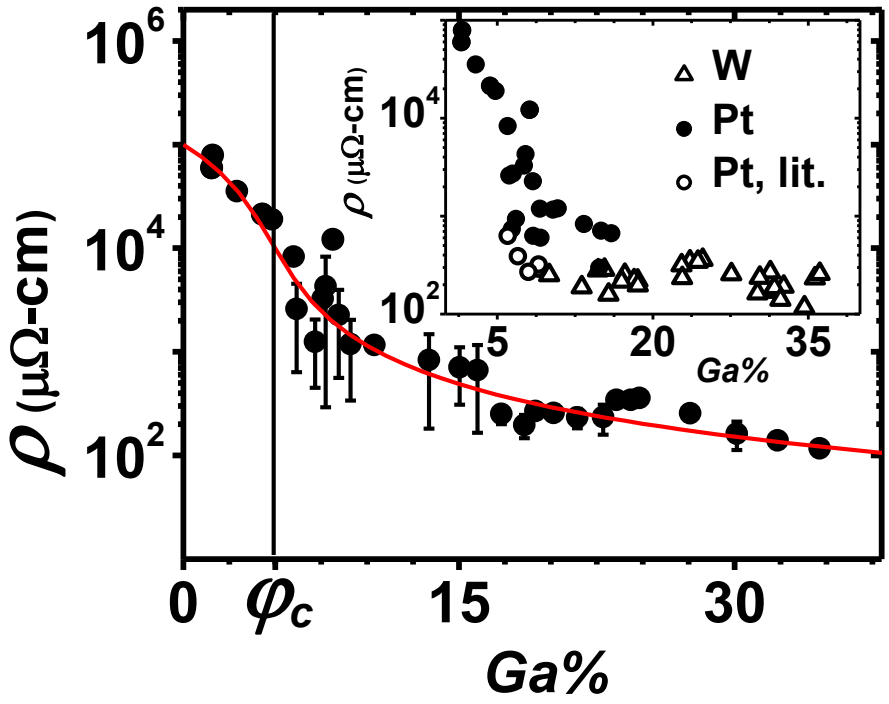

Figure 3.19: The red solid line in represents the fit from the GEM based model to the experimental data (black solid circles). The inset shows the experimental measurements from our report as well as those from literature.

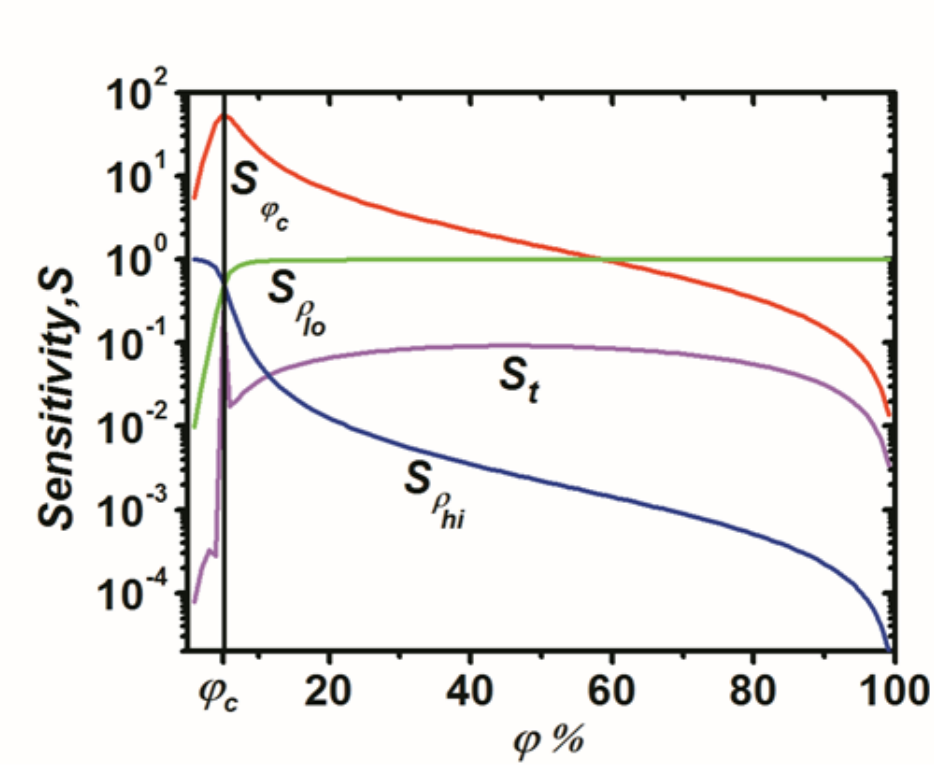

Figure 3.20: The sensitivity (S_α) of the FIB deposited metal resistivity, ρ_m to the fitting parameters, α (=ρ_{hi}, ρ_{lo}, φ_c and t), as a function of the volume fraction, φ

The sensitivity of ρ_m to those fitting parameters are defined[47] by

$$S_\alpha = \left(\frac{d\rho_m}{\rho_m}\right) / \left(\frac{d\alpha}{\alpha}\right) \qquad (3.3.4)$$

which is the ratio of per unit change in the resistivity of the medium to per unit change in the fitting parameters, here α is the fitting parameter and S_α is the sensitivity of ρ_m to α, so $S_\alpha = 0.1$ implies one unit change in α will result in 0.1 unit change in ρ_m. Equation (5) was evaluated and plotted with respect to φ in Figure 3.20. Here it is observed that we can determine φ_c from S_{φ_c} and S_t , as they are highest at φ_c, which is expected, since φ_c determines the atomic % where the transition from the high to low resistivity behavior of the medium occurs, so there will be an abrupt change in ρ_m at φ_c which is reflected in

both S_{φ_c} and S_t . The dependence of ρ_m on ρ_{hi} is expressed by $S_{\rho_{hi}}$, below φ_c , the medium behaves as a high resistivity material, as there are no percolation paths formed, due to smaller atomic % of the low resistivity element, so $S_{\rho_{hi}}$ ~1, so there is a one to one correspondence between ρ_m and ρ_{hi} . Above φ_c, ρ_m approaches toward ρ_{lo} due to the formation of percolating paths and $S_{\rho_{hi}}$ drops orders of magnitude below 1. Similarly, the dependence of ρ_m on ρ_{lo} is expressed by $S_{\rho_{lo}}$, above φ_c, $S_{\rho_{lo}}$~1, so there is a one to one correspondence between ρ_m and ρ_{lo} and below φ_c , $S_{\rho_{lo}}$ abruptly drops below 1, at φ_c, $S_{\rho_{hi}}$ and $S_{\rho_{lo}}$ intersect each other ($S_{\rho_{hi}} = S_{\rho_{lo}}$), which is another way to determine φ_c from $S_{\rho_{hi}}$ and $S_{\rho_{lo}}$.

3.4 Conclusion

In summary, we have shown that the concentration of Ga (the constituent in the ion beam) seems to be the dominant factor in determining the electrical resistance of FIB deposited lines. Extensive analysis has enabled us to also conclude that it is the chemical composition of the deposited material that determines the electrical resistivity and not the FIB beam parameters *per se*. The beam parameters and other effects such as sputtering are all reflected through the chemical composition of the deposition which has been carefully determined through EDS.

The surprising aspect was that the intended metal from the decomposition of the MO precursor does not seem to strongly contribute, presumably due to incomplete precursor decomposition. It may be suggested that, given the limitations with precursor volatility and system stability, the deposition parameters that directly controls Ga^+

concentration should only be considered for tuning the resistivity of FIB metal depositions.

This chapter, in part, is a reprint of material as it appears in the following publications: H Faraby, Michael DiBattista and P R Bandaru, “Percolation of gallium dominates the electrical resistance of focused ion beam deposited metals”, *Applied Physics Letters, Vol.104, Issue 17.*The dissertation author was the primary investigator and author of this material.

Chapter 4 Focused Ion Beam Deposited Insulators

This chapter will discuss the electrical properties of FIB deposited insulators with respect to their elemental composition. It will examine the electrical resistivity and also compare the capacitance per unit area between Ga and Xe based FIB deposited metal-insulator-metal (MIM) structures. Finally it will provide a mathematical model for resistivity variation with Ga concentration of those MIM structures.

4.1 Introduction

Focused Ion Beam (FIB) based depositions are widely used in the semiconductor industry, especially in applications involving repair of integrated circuits (ICs)[48,19] and photo masks, electrical connection and measurement of nanostructures[22,23,24,25] cross section milling and imaging of fabricated devices[20] and transmission electron microscopy (TEM) sample preparation[21].

The ability to deposit insulator material is critical to the modification and repair of ICs as the FIB deposited contact has to be insulated from adjacent wires. However, it is perceived[49,34] that the quality of the insulating layers are effected by implantation of the Ga ion and incorporation of carbon (C). Few prior reports[48,50,51] have investigated different precursors[49] and the relationship of various beam parameters on the growth rate of deposited insulator but the relationship of resistivity variation with material composition was not mentioned.

Here we will present, with experimental evidence, how Ga concentration influences the impedance of FIB deposited insulators.

4.2 Experimental Details

The FIB insulator deposition process involves heating (typically to ~ 50 ^{o}C) the relevant precursor in a gas reservoir attached to the vacuum chamber, after that it is controllably passed, through a gas nozzle, into the chamber. It is thought[34] that the vapor molecules adsorb onto the substrate, and are then decomposed through interaction with the ion beam. Additional oxygen (O_2) gas[34](Figure 4.1) is also supplied along with the precursor to improve film quality while the residual volatile organics are concomitantly removed through vacuum pumping.

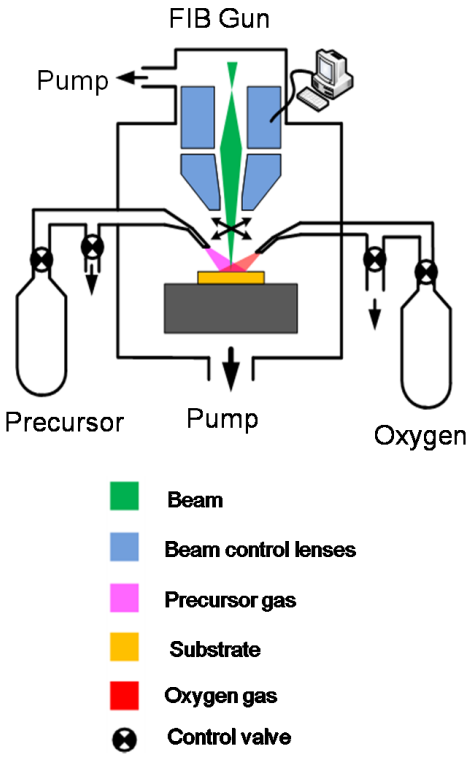

Figure 4.1: FIB based insulator deposition

We focus, on the electrical resistance and capacitance of SiO_2 layers deposited by commercial FIB systems using 1,3,5,7-tetramethylcyclotetrasiloxane (TMCTS): $(HSiCH_3O)_4$ as the precursor gas. During the deposition, the ion beam accelerating voltage was fixed at 50 kV, *e.g.,* to minimize the contribution of the secondary electrons[37]. The beam current (total Ga+ charge/unit time) was fixed at 15nA, the X and Y axis pitch (overlap), which is the separation between the center of adjacent beam spots in X and Y direction respectively, was maintained at 0.24µm for both X and Y directions. The lens 2 voltage, which controls the ion beam spread with respect to the sample surface as a reference (defocus), was held constant at 27376 V. The dwell time, which indicates how long the ion beam resides on a particular spot, was fixed at 0.4µs and refresh time –

time interval between two consecutive scan was 3ms for all the depositions. Two different precursor gas vapor pressure, *i.e.* 0.55 Torr and 0.95 Torr was used for our experiment. The O_2 gas vapor pressure was varied from 0 Torr to 3.5 Torr.

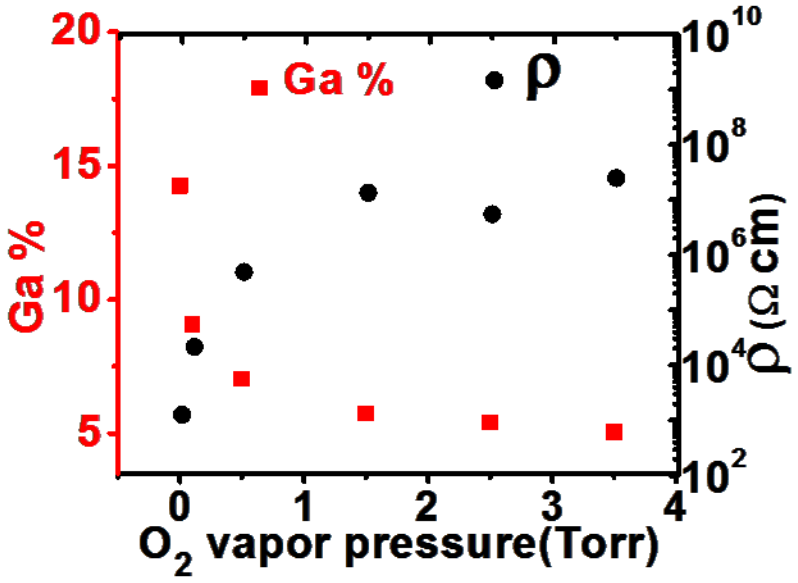

Figure 4.2: Ga% and ρ vs O_2 vapor pressure

Figure 4.2 depicts how the resistivity and Ga concentration varies with the O_2 gas vapor pressure. It indicated that we can control both the resistivity and Ga concentration by changing the O_2 gas vapor pressure. The chemical composition of all the constituent elements in the deposited SiO_2 layers was quantitatively analyzed by energy dispersive spectroscopy[37] (EDS) following all the standard practices. The ratio of EDS peak intensities of the Si, Ga, C and O peaks, to the background intensity, were used to determine the elemental concentrations in the deposited insulator layers using ZAF (Z: atomic number, A; absorption factor, F: fluorescence factor) based matrix corrections.

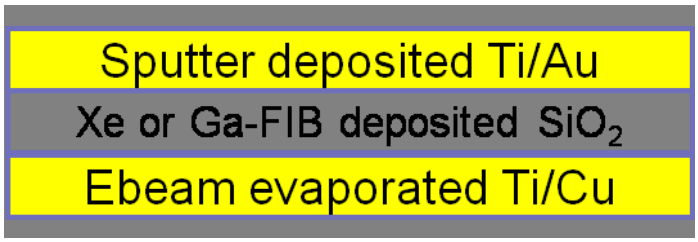

Figure 4.3: Schematic of the device structure

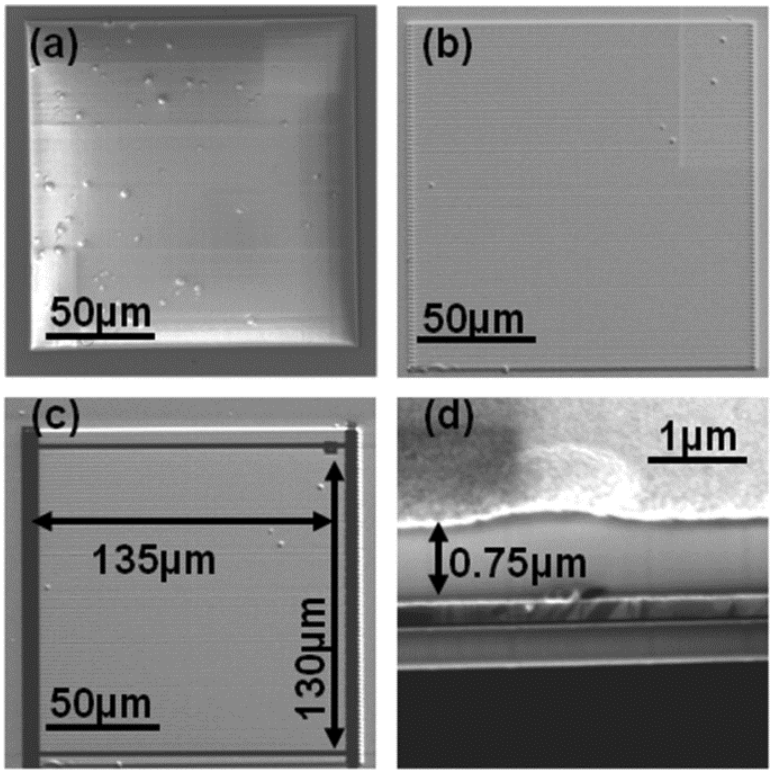

Figure 4.4: SEM image of a metal-insulator-metal (MIM) structure after (a) insulator layer deposition, (b) top contact (Ti/Au) sputtering, (c) milling top contact on the edges of the deposition to isolate the top contact from the bottom contact and to measure *w* and *l* and (d) milling a cross-section to measure *h*.

The insulator layers (Figure 4.4(a)) were deposited on a Ti/Cu coated SiO_2/Si wafer, the Ti/Cu layer was used as the bottom electrode. The top electrode (Figure 4.4(b)) was obtained by sputtering Ti/Au (50nm/150nm) on the insulator layer. Finally the metal – insulator – metal (MIM) (Figure 4.3) structures were fabricated by milling the top

electrode layer (Figure 4.4(c)) along the edges of the deposited insulator. An AC voltage of 100mV with frequency (f) varying from 100kHz to 1MHz was applied across the MIM structures. Agilent B1500A Semiconductor Parameter Analyzer and a commercial probe station was used to measure their impedance and phase shift. The length (l), along with the width (w) (Figure 4.4(c)) and the height (h) (Figure 4.4(d)), of the MIM structures were estimated from scanning electron microscopy (SEM) imaging and FIB cross sectioning.

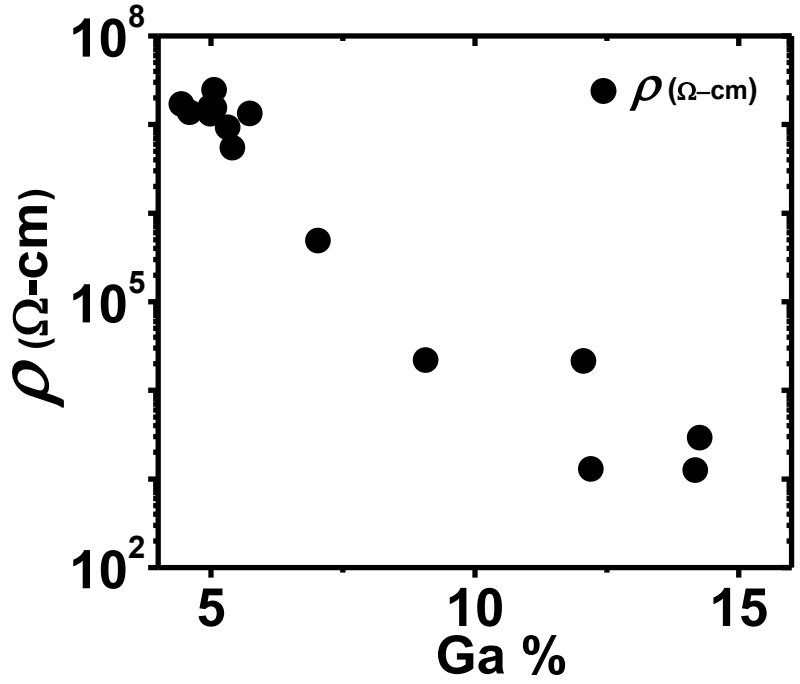

Figure 4.5: The variation of the electrical resistivity (ρ) of the MIM structures with Gallium (Ga)

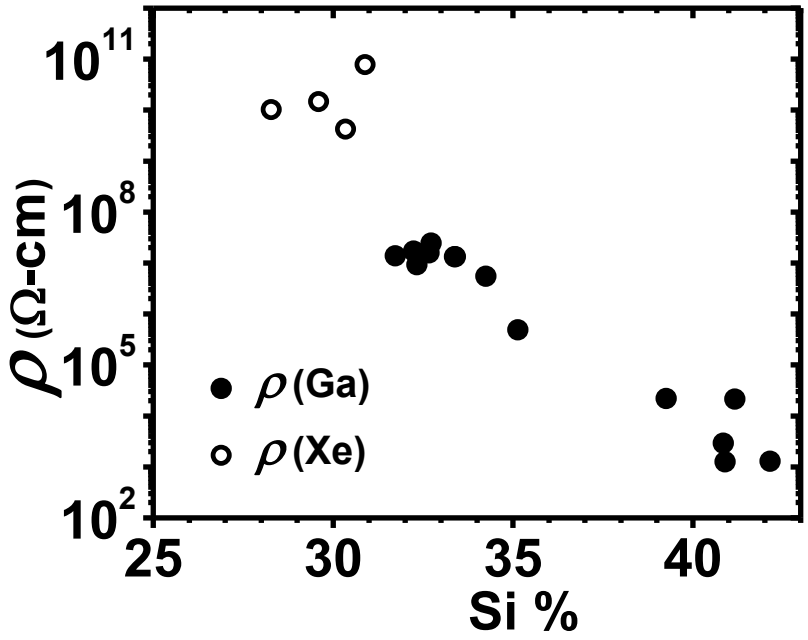

Figure 4.6: The variation of the electrical resistivity (ρ) of the MIM structures (both Xe and Ga FIB) with Silicon (Si)

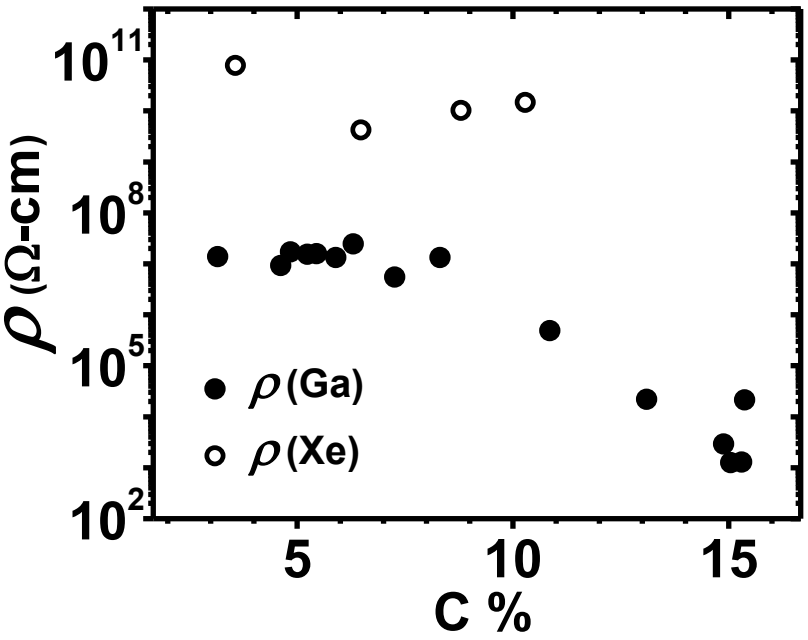

Figure 4.7: The variation of the electrical resistivity (ρ) of the MIM structures (both Xe and Ga FIB) with Carbon (C)

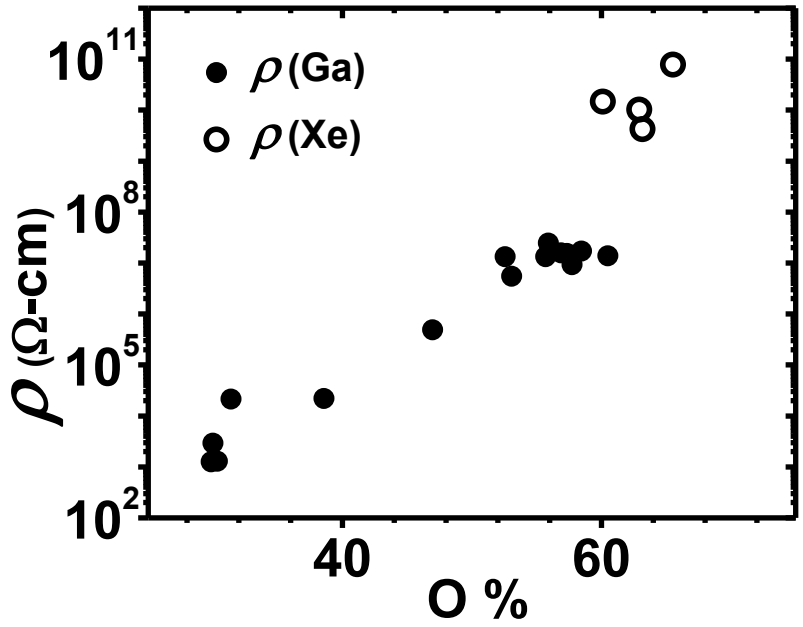

Figure 4.8: The variation of the electrical resistivity (ρ) of the MIM structures (both Xe and Ga FIB) with Oxygen (O)

We plot the estimated resistivity ρ (=*Rwh/l*, the resistance, *R*, is derived from the real part of the impedance) with respect to Ga, Si, C and O atomic % in Figure 4.5,Figure 4.6,Figure 4.7 and Figure 4.8 respectively for Ga and Xe FIB deposited insulators. The ρ relates to the insulating property of the deposition while EDS (used for determining the atomic %) identifies elements independent of their chemical bonding state. For Ga FIB deposited insulators a clear correlation of decreasing ρ, indicating increasingly metallic characteristics, with increasing Ga C and Si was observed, (Figure 4.5, Figure 4.6 and Figure 4.7) indicating a percolative transition to metallic behavior. Among them, Ga has the lowest resistivity[46,52,53] and requires the lowest concentration to tune the resistivity of the deposition.

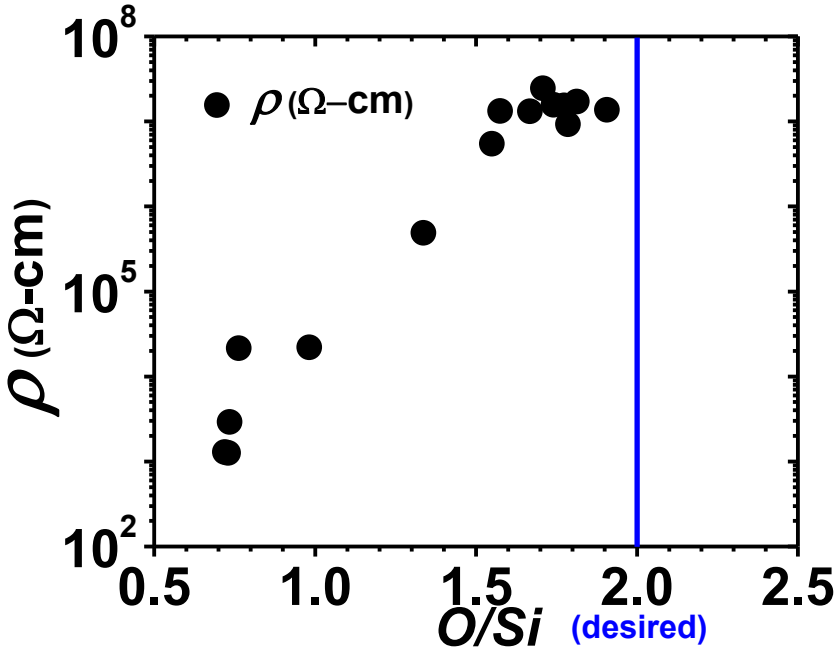

Figure 4.9: Resistivity vs O/Si ratio

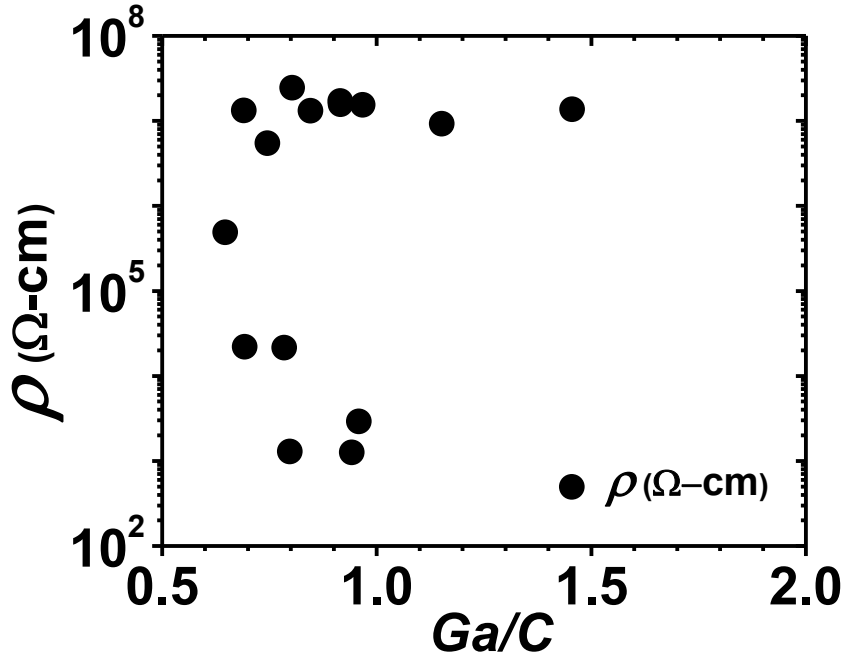

Figure 4.10: Resistivity vs Ga/C

We also plotted ρ with respect to O/Si ratio in Figure 4.9. Ideally for pure SiO_2, O/Si ratio is 2, here we see that when the O/Si ratio is close to 2, ρ is maximum and as ratio moves away from 2(indicating impure SiO_2), ρ decreases abruptly. This suggests that the decrease in resistivity is caused by the impurities present in the SiO_2 layer and not by Si, for Ga based FIB, Ga and C are the impurities. We also plotted ρ versus Ga/C ratio to find out the relative influence of those impurities in Figure 4.10. We see that there is no correlation between the impurities, indicating they are independently affecting the ρ of the SiO_2 layer. In order to find out which element between Ga and C dominates (needs less concentration) to vary the resistivity we performed a sensitivity analysis using the trend of the experimental data (Figure 4.5 and Figure 4.7,Ga only). The sensitivity of ρ with respect to atomic concentration, α is defined through a ratio (S_α) of the unit change in resistivity to unit change in α, *i.e.,*

$$S_\alpha = \frac{\frac{\Delta\rho}{\rho_f}}{\frac{\Delta\alpha}{\alpha_f}}$$

here, $\Delta\rho = |\rho_f - \rho_i|$ and $\Delta\alpha = |\alpha_f - \alpha_i|$ where ρ_f and ρ_i is the ρ at α_f and α_i respectively, subscript f and i denote two consecutive quantities, f representing the higher concentration.

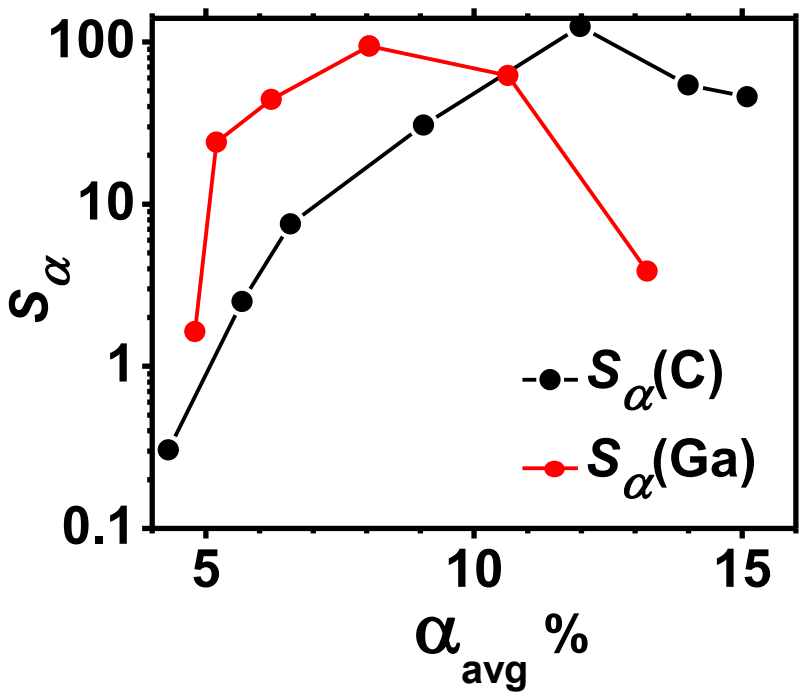

Figure 4.11: S_α vs α_{avg} for Ga(red line) and C(black line) concentration

We plot S_α with respect to α_{avg} $(= (\alpha_f + \alpha_i)/2)$ in Figure 4.11, it is evident that Ga requires less concentration to achieve maximum sensitivity compared to C. The maximum sensitivity represents the maximum change in ρ with a unit change in concentration (which is likely to occur during the transition from insulating to metallic behavior). So we conclude that Ga is the most dominating element for controlling ρ. In order to find the Ga % at which the transition to metallic behavior begins we plot the phase shift, θ $(= tan^{-1}(X_c/R))$ of Ga FIB SiO_2 based MIM structures with respect to Ga atomic % (Figure 4.12). It was observed that at low Ga concentration, $\theta \sim -90^o$ indicating capacitive behavior and after a certain Ga concentration (~6%) θ approaches resistive behavior.

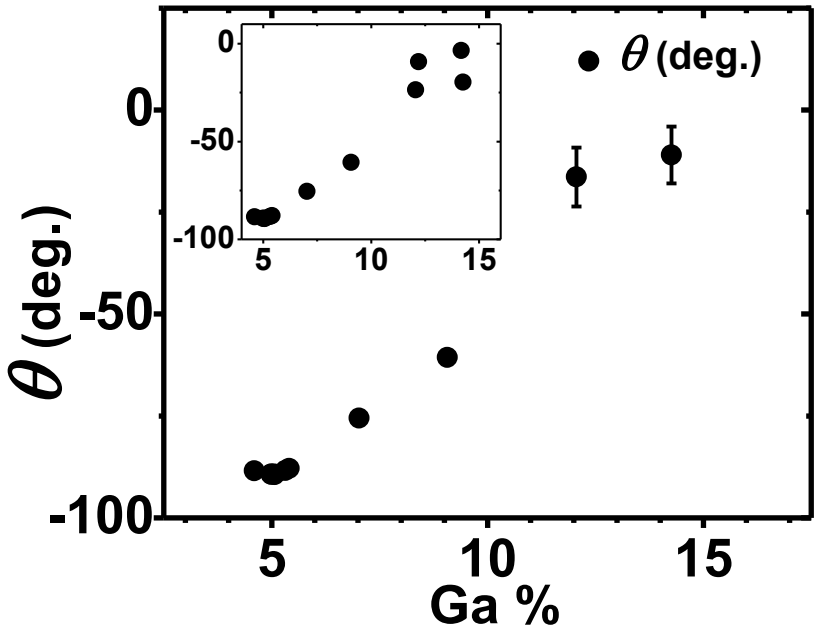

Figure 4.12: Variation of the phase shift (θ) with Gallium (Ga) concentration for Ga based depositions. The inset in shows the experimental measurements from our report

To understand whether Ga would also be a critical parameter to tune the capacitance, we chose to use a FIB system where the influence of Ga could be eliminated. For this purpose, MIM structures with SiO_2 deposited by a Xe based FIB system (FEI Vion PFIB) using 2,4,6,8,10,12-hexamethylcyclohexasiloxane (HMCHS) : $C_6H_{24}O_6Si_6$ as the precursor gas was used. The FIB accelerating voltage was kept constant at 30 kV (maximum achievable by PFIB, to be similar with the Ga ion based FIB)), the pitch fixed to 0μm (for ensuring a uniform rectangular SiO_2 layer of the deposition) and the beam current was varied in the range of 0.2 nA to 15 nA(similar in range with the Ga based FIB). As Xe ions are gaseous at room temperature, this would

preclude their presence in the deposited SiO_2 leaving only C as the major impurity element, whereas in Ga based depositions, both Ga and C are the impurity elements.

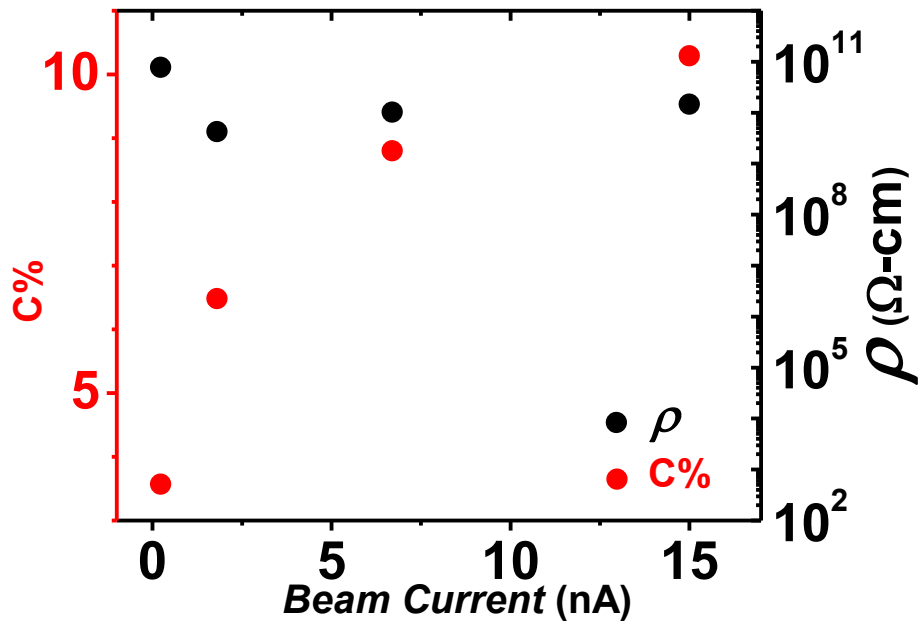

Figure 4.13: C% and ρ vs Beam Current

In Figure 4.13 we plot the resistivity and C% with respect to ρ. We see that the resistivity of Xe FIB based MIMs are relatively constant (Figure 4.6 and Figure 4.13), which helps us understand the effect of Ga.

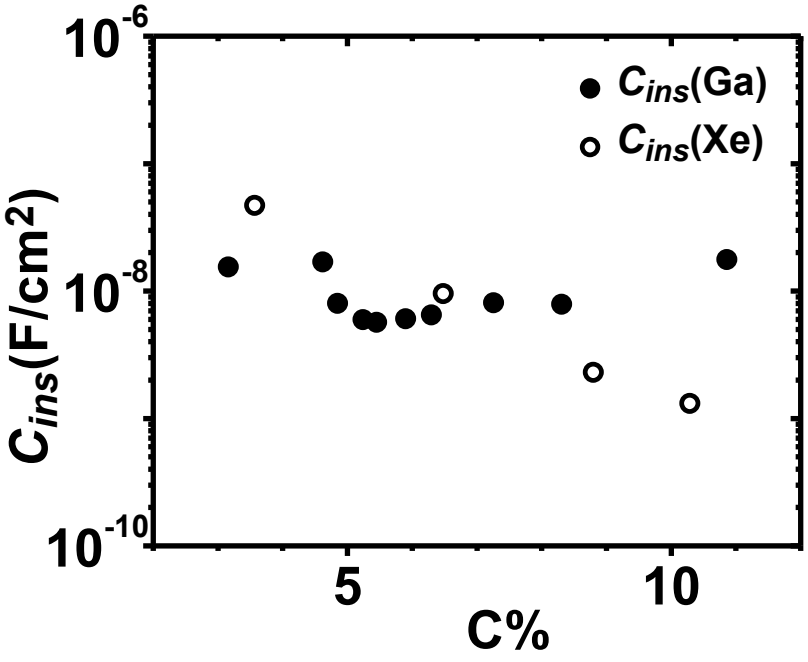

Figure 4.14: The variation of the capacitance per unit area (C_{ins}) of the MIM structures with Carbon(C) concentration for both Ga and Xe ion based depositions

We compared the electrical capacitance (per unit area) C_{ins} (=C/wl), derived from the imaginary part ($X_c=1/j\omega C$, $\omega=2\pi f$) of the impedance of both (Xe and Ga based) type of MIM structures with respect to C atomic %(Figure 4.14). We observed that while for Ga FIB based SiO_2 deposition, the C_{ins} was relatively constant with increasing C atomic %, for Xe FIB based SiO_2 deposition, there was an overall C_{ins} decrease. A tentative explanation for the capacitance decrease, could be based on a reduced ionic polarization[54] in the SiO_2. It is thought/hypothesized[54] that C replaces some of the Si-O bonds in the SiO_2 with Si-C bonds, as the latter has a reduced bond energy (~ 76 kCal/mol compared to 110 kCal/mole for the Si-O bonds) and reduces the effective dielectric permittivity[54]. Such a conclusion is drawn from the relative electronegativity (EN) values of the Si, C

and O values of 1.9, 2.55 and 3.44 respectively, per the Pauling scale[55]. As the polar/ionic nature of a bond depends on the difference in the EN of the constituent atoms , we deduce that Si-C would be less polar than Si-O with a consequent reduced ionic polarization and C_{ins} . On the other hand, for Ga FIB based SiO_2 deposition, the Ga+ ion might introduce additional capacitance, as it was previously reported[56,57,58] that presence of ion in a dielectric layer can introduce capacitive effect in the form of electric double layer capacitance or oxygen-ion binding.

4.3 Theoretical Calculation

In order to understand the percolative behavior of the real part of the impedance of the MIM structures, we theoretically calculated their electrical resistivity using the concept of effective medium theory (EMT). It relates to methodical modeling that outlines the macroscopic properties of composite materials. They are derived from averaging the pristine values of the properties of the constituents that directly make up the composite material. Many theories have been developed which can describe useful properties of the composite material as a whole. In this case, McLachlan's[42,43,44] general effective medium (GEM) based formulations[45], were used to estimate the theoretical resistivity of the Ga based insulators. This theory was developed as a generalization and expansion of Bruggeman's symmetric (symmetrical spherical constituents fill the composite media) and asymmetric (concentrically coated constituents fill the composite media) media theories for binary composites. We predicted that the composite has two components - a low resistivity (ρ_{lo}) component and a high resistivity (ρ_{hi}) component and that the variation observed in Figure 4.5 corresponded to a percolative transition,

where increasing Ga in the FIB deposited insulators decreased the overall electrical resistivity. The following form of the GEM equation was employed:

$$\frac{\varphi\left[(\rho_m)^{\frac{1}{t}}-(\rho_{lo})^{\frac{1}{t}}\right]}{(\rho_m)^{\frac{1}{t}}+\left[\frac{1-\varphi_c}{\varphi_c}\right](\rho_{lo})^{\frac{1}{t}}}+\frac{(1-\varphi)\left[(\rho_m)^{\frac{1}{t}}-(\rho_{hi})^{\frac{1}{t}}\right]}{(\rho_m)^{\frac{1}{t}}+\left[\frac{1-\varphi_c}{\varphi_c}\right](\rho_{hi})^{\frac{1}{t}}}=0 \qquad (4.2.1)$$

In Eqn. (4.2.1), φ is the atomic percentage of the low resistivity component (with φ_c being a critical atomic percentage of ρ_{lo} at which a percolation path is formed through the medium) and t is a critical exponent. Eqn. (4.2.1) reduces to Bruggeman's symmetric and asymmetric media equations in the appropriate limits of the resistivity of the components[43], and can also be viewed as an electrical conductivity/resistivity percolation equation[43]. In this model, we fitted φ_c= 6.5% Ga, as from Figure 4.12 it is seen that the transition from capacitive behavior to resistive behavior begins between 6% to 7% Ga concentration, the value of the exponent t was fitted to 2 corresponding to the standard percolation exponent[59]. The other two parameters ρ_{hi} and ρ_{lo} was fitted to be $5X10^8$ Ω-cm and 20 Ω-cm respectively. Using these parameters Eqn. (4.2.1) was solved numerically with MATLAB for ρ_m and plotted with the experimental data in Figure 4.15.

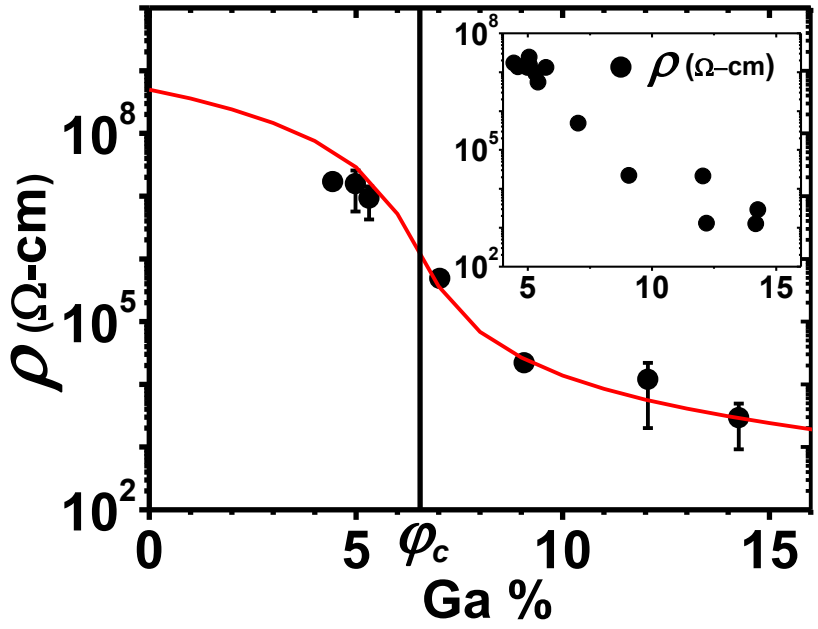

Figure 4.15: The red solid line in represents the fit from the GEM based model to the experimental data (black solid circles). The percolation threshold volume fraction, φ_c is ~ 6.5 atomic % Ga. The inset in shows the experimental measurements from our report

4.4 Conclusion

In summary, we have shown that the concentration of Ga (the constituent in the ion beam) seems to be the dominant factor in determining the electrical resistance of FIB deposited insulators. Also, comparison with Xe based insulators has enabled us to also conclude that it significantly affects their capacitive properties. The beam parameters and other effects such as sputtering are all reflected through the chemical composition of the deposition which has been carefully determined through EDS.

It may be suggested that, Ga^+ concentration should be kept below 6% for optimal capacitive behavior of FIB deposited insulators. The range of beam parameter to achieve Ga concentration below 6% is given in Table 4.1.

Table 4.1: Beam Parameter to achieve Ga concentration below 6%

Beam Energy(kV)	Beam Current(nA)	Pitch (µm)	Lens 2 voltage(V)	Gas 1 (TMCTS)(Torr)	Gas 2 (O_2)(Torr)	Dwell Time(µm)	Retrace Time(µm)	Refresh Time (µm)
50	0.9-15	0.2-0.5	21k-27.4k	0.95	1.5-3.5	0.4	10	3000

Portions of Chapter 4 are a reprint of material as it is under preparation for publication: Faraby H, DiBattista M, Bandaru PR. “Comparison of the electrical capacitance characteristics of SiO_2 deposited through gallium and xenon based focused ion beam systems.” The dissertation author was the primary investigator and author of this material.

Chapter 5 Conclusions

This chapter will summarize the material presented in this dissertation and discuss future directions.

5.1 Summary

The dissertation presented here investigated the inductive properties of CCNTs. The quantum mechanical properties of the CCNTs, due to their nano-scale dimensions, greatly contributed to the total inductance. It was found, through numerical computation, that most of the current challenges in inductor design can be successfully addressed if CCNTs are used as inductor elements. The experimental demonstration of the inductive property is currently limited by poor contacts to the CCNTs during characterization. In order to find a way to create ohmic contacts on CCNTs, FIB based deposition method was extensively analyzed and investigated. A new way to estimate and control the resistivity of FIB deposited metals has been demonstrated and their resistive behavior was described by a mathematical model. We also compared the capacitive properties of Ga and Xe based FIB deposited insulators.

The results and insights obtained from these investigations will greatly enable us to promote CCNTs as a fundamental electrical element such as inductor and to control and estimate the resistive and capacitive properties of FIB deposited metals and insulators which have significant impact on the debug and development of integrated circuits.

5.2 Future Work

For CCNTs, the concept of introducing a core material through the CCNTs could an interesting field of investigation. In conventional inductors introduction of a core material greatly enhance the magnetic inductance. In that regard, whether CCNTs can be synthesized around magnetic material nanowires could be one future are of study, *e.g.* is it possible to grow a CCNT around a Au nanowires.

The biggest question regarding FIB based metals is whether metal (Pt or W) atoms contribute in the resistivity of the FIB deposited metal lines. One of the future experiments to determine this is to study the effect of rapid thermal annealing (RTA) of the FIB deposited metals, because at high temperature the Ga ions should get leave the deposition by vaporization. So the resistivity measured after RTA should be contributed by either from the carbon or the metal atoms present in the deposition.

Another interesting direction of future experiment is to find whether the resistivity of FIB based depositions is precursor independent. From this work, it might seem that Ga is the dominating element, so there is a certain possibility that the resistivity of FIB based depositions (both metal and insulator) might be precursor independent. Of course a very significant amount of experimental verification is required to prove this fact.

References

1. Nieuwoudt A, Massoud Y. Predicting the Performance of Low-Loss On-Chip Inductors Realized Using Carbon Nanotube Bundles. *Electron Devices, IEEE Trans*. 2008;55(1):298–312. doi:10.1109/TED.2007.911091.

2. Scott KL, Hirano T, Yang H, Singh H, Howe RT, Niknejad AM. High-performance inductors using capillary based fluidic self-assembly. *Microelectromechanical Syst J*. 2004;13(2):300–309. doi:10.1109/JMEMS.2003.823234.

3. Ram R. Power electronics. 2010.

4. Poobuapheun N. LNA and mixer designs for multi-band receiver front-ends. *PhD Thesis*. 2009. Available at: http://escholarship.org/uc/item/11n5x36x.pdf. Accessed June 4, 2014.

5. Solar H, Berenguer R, Adin I, Alvarado U, Cendoya I. A Fully Integrated 26.5 dBm CMOS Power Amplifier for IEEE 802.11a WLAN Standard with on-chip "power inductors." *Microw Symp Dig 2006 IEEE MTT-S Int*. 2006:1875–1878. doi:10.1109/MWSYM.2006.249780.

6. INTERNATIONAL TECHNOLOGY ROADMAP FOR RADIO FREQUENCY AND ANALOG / MIXED - SIGNAL TECHNOLOGIES. 2011.

7. Gardner DS, Schrom G, Paillet F, Jamieson B, Karnik T, Borkar S. Review of On-Chip Inductor Structures With Magnetic Films. *IEEE Trans Magn*. 2009;45(10):4760–4766. doi:10.1109/TMAG.2009.2030590.

8. Carleson P. FEI Plasma FIB. 2011.

9. Oh NCL and PN and KMM and DJN and S-H. Engineering metallic nanostructures for plasmonics and nanophotonics. *Reports Prog Phys*. 2012;75(3):36501. Available at: http://stacks.iop.org/0034-4885/75/i=3/a=036501.

10. Ramo S, Whinnery JR, Van Duzer T. *Fields and Waves in Communication Electronics*. 3rd ed. New York; 1993.

11. Plombon JJ, O'Brien KP, Gstrein F, Dubin VM, Jiao Y. High-frequency electrical properties of individual and bundled carbon nanotubes. *Appl Phys Lett*. 2007;90(6):63103–63106. Available at: http://dx.doi.org/10.1063/1.2437724.

12. Burke PJ. Luttinger liquid theory as a model of the gigahertz electrical properties of carbon nanotubes. *Nanotechnology, IEEE Trans*. 2002;1(3):129–144.

13. Li H, Yin W-Y, Banerjee K, Mao J-F. Circuit Modeling and Performance Analysis of Multi-Walled Carbon Nanotube Interconnects. *Electron Devices, IEEE Trans*. 2008;55(6):1328–1337.

14. Naeemi A, Meindl JD. Compact physical models for multiwall carbon-nanotube interconnects. *Electron Device Lett IEEE*. 2006;27(5):338–340. doi:10.1109/LED.2006.873765.

15. Li H, Banerjee K. High-frequency effects in carbon nanotube interconnects and implications for on-chip inductor design. *Electron Devices Meet 2008 IEDM 2008 IEEE Int*. 2008:1–4.

16. Kim J, Nam B, Kim H. A new differential stacked spiral inductor with improved self-resonance frequency. *Microw Opt Technol Lett*. 2011;53(5):1024–1026. doi:10.1002/mop.25900.

17. Grandi G, Kazimierczuk MK, Massarini A, Reggiani U. Stray capacitances of single-layer solenoid air-core inductors. *Ind Appl IEEE Trans*. 1999;35(5):1162–1168. doi:10.1109/28.793378.

18. Grover FW. *Inductance Calculations*. 1st ed. Mineola: Dover Publications, Inc.; 1946.

19. Remes J, Vahakangas J, Uusimaki A. Improving the Yield and Turn-Around Time of Focused Ion Beam Microsurgery of Integrated Circuits by LCVD Method. *Adv Packag IEEE Trans*. 2009;32(2):497–502. doi:10.1109/TADVP.2008.2006911.

20. Pearson C, Bowen L, Lee M-W, et al. Focused ion beam and field-emission microscopy of metallic filaments in memory devices based on thin films of an ambipolar organic compound consisting of oxadiazole, carbazole, and fluorene units. *Appl Phys Lett*. 2013;102(21):213301. doi:10.1063/1.4808026.

21. Argibay N, Brumbach MT, Dugger MT, Kotula PG. Grain boundary diffusivity of Ni in Au thin films and the associated degradation in electrical contact resistance due to surface oxide film formation. *J Appl Phys*. 2013;113(11):114906. doi:10.1063/1.4795768.

22. Fernández-Pacheco A, De Teresa J, Córdoba R, Ibarra M. Metal-insulator transition in Pt-C nanowires grown by focused-ion-beam-induced deposition. *Phys Rev B*. 2009;79(17):174204. doi:10.1103/PhysRevB.79.174204.

23. Bandaru PR, Daraio C, Jin S, Rao a M. Novel electrical switching behaviour and logic in carbon nanotube Y-junctions. *Nat Mater*. 2005;4(9):663–6. doi:10.1038/nmat1450.

24. Gopal V, Radmilovic VR, Daraio C, Jin S, Yang P, Stach E a. Rapid Prototyping of Site-Specific Nanocontacts by Electron and Ion Beam Assisted Direct-Write Nanolithography. *Nano Lett*. 2004;4(11):2059–2063. doi:10.1021/nl0492133.

25. Lee J, Saucer TW, Martin AJ, Tien D, Millunchick JM, Sih V. Photoluminescence imaging of focused ion beam induced individual quantum dots. *Nano Lett*. 2011;11(3):1040–3. doi:10.1021/nl1038902.

26. Granata C, Vettoliere A, Russo R, Fretto M, De Leo N, Lacquaniti V. Three-dimensional spin nanosensor based on reliable tunnel Josephson nano-junctions for nanomagnetism investigations. *Appl Phys Lett*. 2013;103(10):102602. doi:10.1063/1.4819463.

27. Tao T, Ro J, Melngailis J, Xue Z, Kaesz HD. Focused ion beam induced deposition of platinum. In: *The 34th International Symposium on Electron, Ion and Photon Beams*.Vol 8. San ANtonio, Texas (USA): AVS; 1990:1826–1829. Available at: http://dx.doi.org/10.1116/1.585167.

28. Lin J-F, Bird JP, Rotkina L, Bennett P a. Classical and quantum transport in focused-ion-beam-deposited Pt nanointerconnects. *Appl Phys Lett*. 2003;82(5):802. doi:10.1063/1.1541940.

29. Telari K a., Rogers BR, Fang H, Shen L, Weller R a., Braski DN. Characterization of platinum films deposited by focused ion beam-assisted chemical vapor deposition. *J Vac Sci Technol B Microelectron Nanom Struct*. 2002;20(2):590. doi:10.1116/1.1458958.

30. Shedd GM, Lezec H, Dubner AD, Melngailis J. Focused ion beam induced deposition of gold. *Appl Phys Lett*. 1986;49(23):1584–1586.

31. Della Ratta AD, Melngailis J, Thompson C V. Focused-ion beam induced deposition of copper. In: *Proceedings of the 16th international symposium on electron, ion, and photon beams*.Vol 11. San Diego, California (USA): AVS; 1993:2195–2199.

32. Utke I, Hoffmann P, Berger R, Scandella L. High-resolution magnetic Co supertips grown by a focused electron beam. *Appl Phys Lett*. 2002;80(25):4792. doi:10.1063/1.1489097.

33. Langfischer H, Basnar B, Hutter H, Bertagnolli E. Evolution of tungsten film deposition induced by focused ion beam. *J Vac Sci Technol A Vacuum, Surfaces, Film*. 2002;20(4):1408–1415. Available at: http://dx.doi.org/10.1116/1.1486230.

34. Utke I, Hoffmann P, Melngailis J. Gas-assisted focused electron beam and ion beam processing and fabrication. *J Vac Sci Technol B Microelectron Nanom Struct*. 2008;26(4):1197–1276. Available at: http://dx.doi.org/10.1116/1.2955728.

35. Tao T, Ro J, Meingaiiis J, Xue Z, Kaesz HD. Focused ion beam induced deposition of platinum. 1990;8(6):1826–1829.

36. Langford RM, Wang T-X, Ozkaya D. Reducing the resistivity of electron and ion beam assisted deposited Pt. *Microelectron Eng*. 2007;84(5-8):784–788. doi:10.1016/j.mee.2007.01.055.

37. Goldstein J, Newbury DE, Joy DC, et al. *Scanning Electron Microscopy and X-ray Microanalysis*. 3rd ed. New York, NY: Springer; 2007.

38. Wendt M, Schmidt A. Improved reproducibility of energy-dispersive X-ray microanalysis by normalization to the background. *Phys status solidi*. 1978;46(1):179–183. doi:10.1002/pssa.2210460121.

39. Langfischer H, Basnar B, Hutter H, Bertagnolli E. Evolution of tungsten film deposition induced by focused ion beam. *J Vac Sci Technol A Vacuum, Surfaces, Film*. 2002;20(4):1408. doi:10.1116/1.1486230.

40. Utke I, Moshkalev S, Russell P, eds. *Nanofabrication Using Focused Ion and Electron Beams: Principles and Applications*. Oxford University Press, USA; 2012.

41. Li-jian L, Jia-ji W. Investigation of deposited Pt films induced by Focused Ion Beam. *Solid-State Integr Technol 2001 Proceedings 6th Int Conf*. 2001;2:1087–1090 vol.2. doi:10.1109/ICSICT.2001.982087.

42. McLachlan DS. A quantitative analysis of the volume fraction dependence of the resistivity of cermets using a general effective media equation. *J Appl Phys*. 1990;68(1):195–199.

43. McLachlan DS. An equation for the conductivity of binary mixtures with anisotropic grain structures. *J Phys C Solid State Phys*. 1987;20(7):865. Available at: http://stacks.iop.org/0022-3719/20/i=7/a=004.

44. McLachlan DS. Equations for the conductivity of macroscopic mixtures. *J Phys C Solid State Phys*. 1986;19(9):1339. Available at: http://stacks.iop.org/0022-3719/19/i=9/a=007.

45. Landauer R. Electrical conductivity in inhomogeneous media. *AIP Conf Proc*. 1978;40:2–45.

46. Powell RW. The Electrical Resistivity of Gallium and Some Other Anisotropic Properties of this Metal. *Proc R Soc Lond A Math Phys Sci*. 1951;209(1099):525–541. doi:10.2307/98833.

47. Gundrum B, Cahill D, Averback R. Thermal conductance of metal-metal interfaces. *Phys Rev B*. 2005;72(24):245426. doi:10.1103/PhysRevB.72.245426.

48. Abramo M, Adams E, Gibson M, Hahn L, Doyle a. Focused-ion-beam-induced insulator deposition at decreased beam current density. *1997 IEEE Int Reliab Phys Symp Proceedings 35th Annu*. 1997:66–71. doi:10.1109/RELPHY.1997.584240.

49. Edinger K. Study of precursor gases for focused ion beam insulator deposition. *J Vac Sci Technol B Microelectron Nanom Struct*. 1998;16(6):3311. doi:10.1116/1.590497.

50. Young RJ. Focused ion beam insulator deposition. *J Vac Sci Technol B Microelectron Nanom Struct*. 1995;13(6):2576. doi:10.1116/1.588026.

51. Perentes a., Hoffmann P. Focused Electron Beam Induced Deposition of Si-Based Materials From SiOxCy to Stoichiometric SiO2: Chemical Compositions, Chemical-Etch Rates, and Deep Ultraviolet Optical Transmissions. *Chem Vap Depos*. 2007;13(4):176–184. doi:10.1002/cvde.200606583.

52. Paul W, Pearson GL. Pressure Dependence of the Resistivity of Silicon. *Phys Rev*. 1955;98(6):1755–1757. Available at: http://link.aps.org/doi/10.1103/PhysRev.98.1755.

53. Blue MD, Danielson GC. Electrical Properties of Arc-Evaporated Carbon Films. *J Appl Phys*. 1957;28(5):583. doi:10.1063/1.1722807.

54. Kim HJ, Shao Q, Kim Y-H. Characterization of low-dielectric-constant SiOC thin films deposited by PECVD for interlayer dielectrics of multilevel interconnection. *Surf Coatings Technol*. 2002;171(1-3):39–45. doi:10.1016/S0257-8972(03)00233-0.

55. Pauling L. *The Nature of the Chemical Bond An Introduction to Modern Structural Chemistry*. 3rd ed. Ithaca, NY: Cornell University Press; 1960:88–95.

56. Liu Y, Guan P, Zhang B, Falk ML, Katz HE. Ion Dependence of Gate Dielectric Behavior of Alkali Metal Ion-Incorporated Aluminas in Oxide Field-Effect Transistors. *Chem Mater*. 2013;25(19):3788–3796. doi:10.1021/cm4012537.

57. Kruempelmann J, Mariappan CR, Schober C, Roling B. Electrochemical double layers at the interface between glassy electrolytes and platinum: Differentiating between the anode and the cathode capacitance. *Phys Rev B*. 2010;82(22):224203. doi:10.1103/PhysRevB.82.224203.

58. Mariappan CR, Heins TP, Roling B. Electrode polarization in glassy electrolytes: Large interfacial capacitance values and indication for pseudocapacitive charge storage. *Solid State Ionics*. 2010;181(19-20):859–863. doi:10.1016/j.ssi.2010.05.011.

59. Stauffer D, Aharony A. *Introduction to Percolation Theory*. 2nd ed. London: Taylor and Francis; 2003.